Reconfigurable Intelligent Surface Relying on Low-complexity Joint Sector Non-diagonal Structure

YINUO DONG, QINGCHAO LI ,(GRADUATE STUDENT MEMBER, IEEE), SOON XIN NG, (SENIOR MEMBER, IEEE), AND MOHAMMED EL-HAJJAR, (SENIOR MEMBER, IEEE)

[1]School of Electronics and Computer Science, University of Southampton, SO17 1BJ, United Kingdom
CORRESPONDING AUTHOR: M. EL-HAJJAR (e-mail: meh@ecs.soton.ac.uk)

ABSTRACT In recent years, research on reconfigurable intelligent surface (RIS) has received extensive attention due to its capability to manipulate the propagation of incident electromagnetic waves in a programmable manner to smartly configure the channel environment, thereby optimizing the overall performance of the system. Several RIS architectures have been proposed, including simultaneous transmitting and reflecting RIS (STAR-RIS) and beyond diagonal RIS (BD RIS) architectures. Compared to the conventional RIS architecture, these structures offer broader service ranges and enhanced performance, albeit accompanied by more complex circuit design and higher computational overhead. In this paper, we design a multi-sector RIS joint service model based on the BD RIS architecture and we compare the corresponding system rates, circuit complexity, and gains provided by different architectures. Additionally, we derive the theoretical receive power for the proposed model based on non-diagonal and diagonal phase shift optimization methods, demonstrating that the total rate of the non-diagonal group connected architecture approaches the theoretical values of a fully connected architecture. Theoretical analysis based on the gains between different models under various user-RIS positions confirm that the multi-sector RIS joint service model can achieve $30\% - 100\%$ gains as the users' positions change, while also saving on the overall hardware costs of the RIS system design. Furthermore, we explore the optimal trade-off between the performance and circuit complexity among different architectures. Simulation results show that performance versus complexity trade-off of the different considered architectures.

INDEX TERMS Reconfigurable intelligent surface (RIS), beamforming, beyond diagonal RIS, group-connected RIS, non-diagonal RIS.

I. INTRODUCTION

RIS is an artificial two-dimensional (2D) surface equipped with a large number of low-cost passive components, enabling large-scale communications at lower hardware cost and power consumption [2]. The propagation of the wireless signal incident on the RIS can be adjusted by customizing the phase response of each component and hence, RIS can facilitate "Smart Radio Environments (SREs)" [3], [4].

In the state-of-the-art RIS beamforming designs [5]- [11], the design goals mainly focused on minimizing the transmit power, maximizing the channel capacity, or maximizing the signal to interference plus noise ratio (SINR), when the channel state information (CSI) is perfectly known at the transmitter side. Explicitly, Wu and Zhang [5] proposed a centralized algorithm based on the semi-definite relaxation (SDR) technique, where the base station (BS) and the RIS independently adjust the transmit beamforming and the RIS phase shift in an alternating manner to minimize the downlink transmit power in RIS-assisted MIMO systems. Additionally, [6] and [7] used the low-complexity alternating direction method alternating direction method of multipliers (ADMM) to replace the SDR, and realize the joint optimization of the RIS phase shift matrix and the active beamforming at the base station. Furthermore, an optimization algorithm suitable for both discrete phase-shift RIS and continuous phase-shift RIS has been proposed in [6], which realizes multi-user weighting and rate maximization in multiple input multiple output (MIMO) scenarios. Specifically, the authors of [7] decomposed the effective channel between the source and the destination

using the classical singular value decomposition (SVD) after the ADMM optimization to obtain the precoding matrix at the source, and hence realize the maximum sum-path gain of the RIS-assisted MIMO system.

Under the constraint of a user's signal-to-noise ratio (SNR), the authors in [8] solved the problem of minimizing the total transmit power at the transmitter end by jointly optimizing the transmit beamforming of the active antenna array at the BS and the continuous phase shift optimization of the RIS. If the phase shift is discrete, the quantized continuous solution is near-optimal, or a greedy iterative search can be used. Additionally, in [9], an efficient algorithm was proposed to alternately optimize the power allocation at the BS and the passive beamforming at the RIS in an iterative manner, which improves the orthogonal frequency-division multiplexing (OFDM) link rate performance.

However, the RIS structure in [5]-[11] has only one reflective surface, which means that the RIS can only serve users roaming within 180° in front of the RIS plane. Specifically, to receive signals from reflective-only RIS, the user must be on the same side as the BS. To alleviate this shortcoming and facilitate a more flexible system design of RIS-assisted networks, authors in [12] and [13] proposed a new concept of simultaneous transmitting and reflecting RIS (STAR-RIS). In [12], the wireless signal incident on the STAR-RIS element from both sides of the surface are divided into two parts: one part (reflection signals) is reflected onto the same space as the incident signals, which is the reflection space and the other part (transmission signals) is transmitted to the opposite space as the incident signal. By controlling the current and magnetic currents of the STAR-RIS elements [12], the transmitted and reflected signals can be reconfigured by two usually independent coefficients: the transmission coefficient and the reflection coefficient. Therefore, a highly flexible full-space smart radio environment (SRE) can be realized. In [13] three practical STAR-RIS operation protocols were proposed, namely energy splitting, mode switching, and time switching. Based on the proposed protocols, a series of promising application scenarios for integrating STAR-RIS into next-generation wireless networks have been proposed [14]. Moreover, some other RIS architectures such hybrid RIS and omni-RIS are also proposed to support multiple scenarios. Guo *et al.* [15] propose a novel hybrid RIS architecture that integrates a wireless beacon to enhance channel estimation accuracy by proactively detecting partial channel state information. This design addresses the challenge of angular distortion typically found in fully-passive RIS systems and significantly reduces the pilot overhead through a tailored three-phase frame structure involving broadcasting, estimation, and calibration phases. Besides, Chen *et al.* [16] introduce an advanced beamforming strategy for omni-RIS for vehicular communications vehicular communications. The work leverages a robust beamforming framework to optimize the system performance under non-ideal conditions such

as non-convex outage probabilities, significantly enhancing the reliability and effectiveness of vehicular communication systems through the active RIS design.

Currently, as research on RIS continues to advance, there is a growing awareness of the significant impact that the angles of incidence and reflection of signals on RIS elements have on the signal pathloss [17], [19]. The pathloss of the reflected signals by the RIS is primarily determined by the angle between the signal and the normal of the RIS plane, which is known as the elevation angle. [18] showed that the pathloss is minimized when the incident signal is perpendicular to the RIS surface, and it becomes nearly infinite when the incident signal is close to a 90-degree angle relative to the normal of the RIS plane. Therefore, based on these pathloss models, when the angle between the user position of STAR-RIS surface and the line connecting the reflecting surface is very small, the reflecting surface can hardly play a communication role, which can cause a series of problems such as signal interruption and reduced degrees of freedom.

Additionally, in conventional RIS structures, it is assumed that an incident signal that hits a particular element can only be reflected from that element after being adjusted for phase shift. In other words, there is no cooperation among RIS elements. Therefore, the phase-shift matrix in these designs has a diagonal structure, which cannot fully utilize the potential of RIS to improve the system performance. Shen *et al.* [20] studied the cooperation among RIS elements and proposed a fully-connected and group-connected RIS architecture. The related theoretical analysis and simulation results showed that when considering SISO systems, these architectures can significantly increase the received signal power compared with the conventional RIS structure. Li *et al.* [21] proposed a novel RIS architecture based on non-reciprocal connections, in which a signal impinging on a specific element can be reflected from another element after phase-shift adjustment. As a result, the phase-shift matrix can have an asymmetric and non-diagonal property. The non-diagonal architecture provides flexibility in configuring the RIS structure to enhance the system's performance [27]. Moreover, Li *et al.* considered a stereoscopic structure of RIS [29], called beyond diagonal RIS. In [29], the user can communicate with one sector in the corresponding direction. With the fixed total number of RIS elements, more sectors will reduce the number of elements in each sector. Hence, when a RIS is divided into more sectors, the number of RIS elements serving each user decreases. In this case, the pathloss brought by the smaller reflection angle will be greatly offset by the reduced number of RIS elements. *Hence, in our proposed model, the group connection and non-diagonal connection are combined in a multi-sector RIS architecture, so that the signals in different sectors can be transmitted to other sectors. Then, an asymmetric, non-diagonal phase shift matrix is realized, which can enable*

TABLE 1. Novelty comparison with the literature

	Our paper	[5]	[6]	[7]	[8]	[12]	[13]	[17]	[18]	[19]	[21]	[29]
Beamforming Design	✓	✓	✓	✓	✓	✓	✓				✓	✓
Multi-user support	✓					✓					✓	✓
Cooperation among RIS elements	✓							✓	✓	✓	✓	✓
Full coverage	✓							✓	✓	✓		✓
Angle-related pathloss model	✓							✓	✓	✓		✓
Correlated channel model	✓											
Multi-sector Cooperation	✓											

an improved performance compared to the conventional connection method and group connection method.

The model proposed in this paper can be widely applied to numerous indoor and outdoor environments such as shopping malls, stations, and public squares, enabling a single-side deployment of the BS that can serve multiple users omni-directionally, with the support of multi-sector RIS. Furthermore, deploying multi-sector RIS at busy central locations can facilitate vehicular communications and enhance the connectivity of user equipment. This approach suits any scenario requiring omnidirectional communication where the BS cannot be deployed on multiple sides. Depending on the trade-offs between hardware complexity and channel rates, different models presented in this study can be flexibly selected to meet specific needs.

In this paper, we propose a novel multi-sector RIS structure based on the beyond diagonal RIS architecture, where the user always communicates with half of the sectors of the RIS regardless of the number of elements in each sector. This can provide flexibility in terms of configuring the RIS structure for enhancing the achievable performance. We also propose the joint beamforming and phase shift design by employing an alternative optimization and singular value decomposition (SVD) for single-user multiple input single output (MISO) systems and multi-user MIMO systems, respectively. The theoretical analysis and simulation results demonstrate that our proposed RIS architecture achieves a better sum rate performance than the conventional RIS architecture and the STAR-RIS. Against this background, the novel contributions of this paper are summarized as follows:

• We propose novel RIS architectures based on the beyond diagonal RIS concept. We design a multi-sector joint service method for a single user based on the beyond diagonal RIS structure, and propose the corresponding circuit design and beamforming techniques. Simulation results show that, compared to the single-sector service for a user with the beyond diagonal RIS design [29], our proposed multi-sector joint service structure can achieve a gain improvement ranging from 30% to 100%, depending on the roaming location of the user, relative to the structures described in [29].

• We propose two types of connections in the multi-sector RIS architecture. The full-link and opposite-link structures are considered in the horizontal connection design of the beyond diagonal RIS structure. Additionally, in the vertical connection design, we apply the non-diagonal RIS architecture based on [21]. We design the group-connected scheme within each sector, employing the non-diagonal architecture in each group. Our proposed non-diagonal RIS structure is designed for finding a trade-off between the hardware complexity and the achievable performance. Based on our theoretical analysis and simulation results, we conclude that our proposed structure achieves a performance comparable to the fully connected structure in [29] albeit with significantly lower overall complexity.

• We jointly design the beamforming and phase shift matrix by alternating optimization and SDR methods of the proposed architecture for maximizing the achievable rate in both MISO and MIMO systems.

• We provide both theoretical and simulation results for characterizing the performance of our proposed RIS architecture, which has improved performance and lower complexity compared to the conventional RIS architecture, the STAR RIS and the beyond diagonal RIS.

Table 1 compares and contrasts the novelty of this paper with the state-of-the-art literature. The rest of this paper is organized as follows. In Section II, we present the system model. The RIS architecture and beamforming design methods are formulated in Section III and Section IV, respectively. The theoretical analysis is presented in Section V and the simulation results are shown in Section VI. Finally, we conclude in Section VII.

Notations: Vectors and matrices are denoted by boldface lower and upper case letters, respectively, $(\cdot)^{\mathrm{T}}$ and $(\cdot)^{\mathrm{H}}$ represent the operation of transpose and Hermitian transpose, respectively. $\angle a$ represent the angle of the complex scalar a, $\mathbf{1}_{n \times m}$ represent the $n \times m$ all-one matrix and $\mathbf{0}_{n \times m}$ represent the $n \times m$ all-zero matrix. $\mathbf{1}_n$ represents the $n \times 1$ all-one vector and $\mathbf{0}_n$ represents the $n \times 1$ all-zero vector. $\mathbb{R}^{m \times n}$ and $\mathbb{C}^{m \times n}$ denotes the space of $m \times n$ real-valued and complex-valued matrices, respectively. $\mathbb{E}\{x\}$ represent the expectation of variable x. $\mathrm{Diag}\{a_1, a_2, \cdots, a_N\}$ denotes a diagonal matrix with the diagonal elements being the elements of $[a_1, a_2, \cdots, a_N]$ in order. $\mathcal{CN}(\boldsymbol{\mu}, \boldsymbol{\Sigma})$ is a circularly symmetric complex Gaussian random vector with the mean $\boldsymbol{\mu}$ and the covariance matrix $\boldsymbol{\Sigma}$. $\mathbf{A} \succeq 0$ means $\mathbf{A}$ is a semi-definite matrix, $\mathbf{I}_n$ represents the $n \times n$ identical matrix.
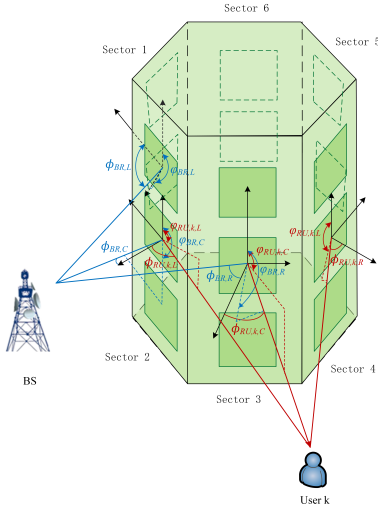
FIGURE 1. RIS structure with $L = 6$ sectors employing $N = 18$ elements.
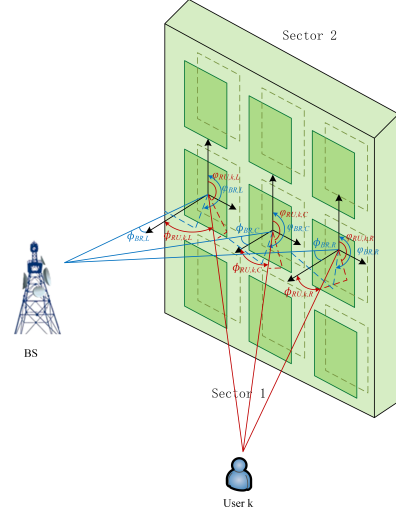
FIGURE 2. STAR RIS with $L = 2$ sectors employing $N = 18$ elements.

$\mathrm{mod}(\cdot, \cdot)$ denotes the modulus and $\lceil \cdot \rceil$ denotes round up of the value, respectively. $\mathcal{M}$ represent the mapping sequence between two sets. $\mathbf{R}_{(p,q)}$ represent the (p, q)th element of the matrix $\mathbf{R}$. $\mathbf{V}^{(1:K)}$ represent the first K columns of matrix $\mathbf{V}$. $\mathrm{Tr}(x)$, $\mathrm{Rank}(x)$ and $|x|$ represent the trace, rank and determinant of matrix x, respectively.

II. SYSTEM MODEL

In this section, we introduce the system model, which is a three-dimensional reflective surface composed of multiple parts of conventional planar RIS connected by a certain angle. In Figure 1, we show a three-dimensional structure composed of six planar RIS in the shape of a hexagon[1]. Compared with the conventional RIS, it can cover the surrounding 360-degree environment, ensuring greater coverage. Figure 2 shows the STAR-RIS system model, which can be considered as a special case of the proposed model using two sectors and is capable of providing wider coverage than the reflective RIS architecture and is considered as a benchmark scheme for our proposed work.

As shown in Figure 1, we consider the BS and the users communicate in the far field, where both the BS and the users can communicate with multiple sectors in our proposed architecture. This ensures that the system can provide better services to users with the same number of RIS elements, and ensures that the number of elements serving each user does not change with the variation of the number of sectors L. When the user roams, each sector is responsible for the sector area corresponding to an angle of $2\pi/L$ directly in front of it. This sector serves as the central sector for the user, with $L/2 - 1$ sectors on both side acting as side sectors. These side sectors cooperate with the central sector to provide service to the user.

---

[1]The six sectors is an example and any number of sectors can be applied in our proposed structure.

In this paper, we consider the RIS-aided downlink MISO and MIMO communications in a single-cell network. The BS is located in a fixed position that is always capable of communicating with 3 sectors in the proposed RIS model in Figure 1. The RIS is deployed to transmit the signal to users, where each user also communicates with 3 sectors in the RIS. Note that the RIS sectors communicating with the BS and the users may overlap totally, partially, or not overlap at all.

In this system, the RIS is employed to assist communication from a BS with M transmit antennas to K single-antenna users, where the RIS deploys L (an even number) sectors with a total of $N = N_x \times N_y$ elements. N_x refers to the number of RIS elements in the horizontal direction and N_y represent the number of RIS elements in the vertical direction in each sector. In this paper, for simplicity we consider $N_x = L$, although any number N_x different from L can be employed. The RIS is equipped with a controller to adjust the group connections and phase shifts of the RIS elements. To characterize the theoretical performance of the RIS-aided system, we assume that all the channel state information (CSI) is perfectly known at the BS. The CSI can be achieved from channel estimation, where there are many works related to channel estimation in RIS-aided systems such as [24] [25] [26].

The baseband equivalent channels from the BS to the RIS and that from the RIS to K users are denoted as $\mathbf{G} \in \mathbb{C}^{N \times M}$ and $\mathbf{H} \in \mathbb{C}^{K \times N}$, respectively. Here, the RIS is a passive reflecting device that can configure the phase and amplitude of the incident signal. Let's define a diagonal matrix $\boldsymbol{\Theta} = \mathrm{Diag}\{\beta_1 e^{j\theta_1}, \ldots, \beta_N e^{j\theta_N}\}$ to represent the reflection coefficients matrix of the RIS, where $\beta_n \in [0, 1]$ and $\theta_n \in [0, 2\pi)$ represent the amplitude and phase shift of the nth elements of the RIS, respectively. In this paper, we set $\beta_n = 1$ to realize full energy transfer.

Additionally, we design a BS precoding scheme where the kth user is assigned with a beamforming vector $\mathbf{w}_k$. Hence, the total beamforming matrix at the BS is denoted as $\mathbf{W} = [\mathbf{w}_1, \mathbf{w}_2, \ldots \mathbf{w}_K] \in \mathbb{C}^{M \times K}$. The beamforming scheme design is detailed in Section IV.

The system model can be represented as

$$\mathbf{y} = \sqrt{P_t}\mathbf{H}\mathbf{\Theta}\mathbf{G}\mathbf{W}\sqrt{\mathbf{\Lambda}}\mathbf{x} + \mathbf{n}, \tag{1}$$

where $\mathbf{x} \in \mathbb{C}^{K \times 1}$ is the transmit signal, $\mathbf{n} \sim \mathcal{CN}(\mathbf{0}_K, \sigma_n^2 \mathbf{I}_K) \in \mathbb{C}^{K \times 1}$ is the additive white Gaussian noise (AWGN) and $\mathbf{y} \in \mathbb{C}^{K \times 1}$ is the received signal. Furthermore, P_t is the transmit power at the BS, $\mathbf{\Lambda} = \text{Diag}\{\lambda_1, \ldots, \lambda_K\}$ is the power allocation matrix, with λ_k representing the power allocated to the kth user, that satisfies $\lambda_1 + \lambda_2 + \ldots + \lambda_K = 1$.

A. Channel model
When the direct link between the BS and the users is blocked, the RIS is used to create a reflective link to connect the users to the BS. The channel $\mathbf{G}$ can be written as $\mathbf{G} = [\mathbf{g}_1, \mathbf{g}_2, \ldots, \mathbf{g}_M]$, where $\mathbf{g}_m \in \mathbb{C}^{N \times 1}(m = 1, 2, \ldots, M)$ represents the channel vector from the mth antenna in the BS to the RIS. The channel matrix from the RIS to the kth user is denoted as $\mathbf{h}_k^{\text{H}} \in \mathbb{C}^{1 \times N}(k = 1, 2, \ldots, K)$, resulting in $\mathbf{H} = [\mathbf{h}_1, \mathbf{h}_2, \ldots, \mathbf{h}_K]^{\text{H}}$. Here, we employ Rician fading distribution for modeling the channel, where we consider spatially correlated channels [28]. Moreover, we consider the pathloss associated with the gain of the RIS and the BS antennas [32].

The Rician channel model from the BS to the RIS and that from the RIS to the kth user is given by

$$\widetilde{\mathbf{G}} = \sqrt{\frac{\kappa_{\mathbf{G}}}{1 + \kappa_{\mathbf{G}}}}\mathbf{G}_{\text{LoS}} + \sqrt{\frac{1}{1 + \kappa_{\mathbf{G}}}}\mathbf{G}_{\text{NLoS}}, \tag{2}$$

$$\widetilde{\mathbf{h}_{\mathbf{k}}}^{\text{H}} = \sqrt{\frac{\kappa_{\mathbf{h}_k}}{1 + \kappa_{\mathbf{h}_k}}}\mathbf{h}_{k\,\text{LoS}}^{\text{H}} + \sqrt{\frac{1}{1 + \kappa_{\mathbf{h}_k}}}\mathbf{h}_{k\,\text{NLoS}}^{\text{H}}, \tag{3}$$

where $\kappa_{\mathbf{G}}$ and $\kappa_{\mathbf{h}_k}$ are Rician factors, $\mathbf{G}_{\text{LoS}} = \mathbf{1}_{N,M}$ and $\mathbf{h}_{k\,\text{LoS}} = \mathbf{1}_N$ are the LoS parts, $\mathbf{G}_{\text{NLoS}} = [\widetilde{\mathbf{g}}_1, \widetilde{\mathbf{g}}_2, \ldots, \widetilde{\mathbf{g}}_M], \widetilde{\mathbf{g}}_M \sim \mathcal{CN}(\mathbf{0}_N, \mathbf{I}_N) \in \mathbb{C}^{N \times 1}$ and $\mathbf{h}_{k\,\text{NLoS}} \sim \mathcal{CN}(\mathbf{0}_N, \mathbf{R}) \in \mathbb{C}^{1 \times N}$ are the non-line-of-sight (NLoS) component of the channel. $\mathbf{R}$ is the spatial correlation matrix represented as [28]:

$$\mathbf{R} = \mathbb{E}\{\mathbf{h}_{kNLoS}\mathbf{h}_{kNLoS}^{\text{H}}\} = \mathbb{E}\{\mathbf{a}(\varphi, \phi)\mathbf{a}(\varphi, \phi)^H\}, \tag{4}$$

where $\mathbf{a}$ is the array response vector denoted as

$$\mathbf{a} = [e^{j\mathbf{k}(\varphi, \phi)^T \mathbf{u_1}}, \ldots, e^{j\mathbf{k}(\varphi, \phi)^T \mathbf{u_N}}]^T, \tag{5}$$

with φ and ϕ representing the azimuth and elevation angle between the RIS surface and the signal, respectively. Furthermore, $\mathbf{u}_n$ is the location of the nth element in the RIS and can be represented as

$$\mathbf{u}_n = \begin{bmatrix} i(n)(s_x + \delta)\sin(\frac{\pi}{L} + (n-1)\frac{2\pi}{L}) \\ i(n)(s_x + \delta)\cos(\frac{\pi}{L} + (n-1)\frac{2\pi}{L}) \\ j(n)(s_y + \delta) \end{bmatrix}, \tag{6}$$

where $i(n) = \text{mod}(n - 1, L)$ and $j(n) = \lceil N/N_y \rceil$, while s_x and s_y are the width and length of each element of the RIS, respectively. Additionally, δ is the distance between the RIS elements.

Furthermore, $\mathbf{k}(\varphi, \phi) \in \mathbb{R}^{3 \times 1}$ is the wave vector represented as [28]:

$$\mathbf{k}(\varphi, \phi) = \frac{2\pi}{\lambda}[\cos(\phi)\cos(\varphi), \cos(\phi)\sin(\varphi), \sin(\varphi)]^T. \tag{7}$$

Finally, the (p, q)th element of $\mathbf{R}$ can be expressed as [30]

$$\begin{aligned} \mathbf{R}_{(p,q)} &= \mathbb{E}\{e^{j\mathbf{k}(\varphi, \phi)^T}(\mathbf{u}_p - \mathbf{u}_q) \\ &= \text{sinc}(\frac{2\|\mathbf{u}_n - \mathbf{u}_m\|}{\lambda}), \qquad n, m = 1, \ldots, N \end{aligned} \tag{8}$$

where $\text{sinc}(x) = \sin(\pi x)/(\pi x)$.

B. Pathloss model
In this section, we present the pathloss model, where we first start with a simple narrow-band down-link model, where the signal is transmitted from the BS to the RIS with only a single reflective surface, and then reflected to a user. Consider that all antennas used in the model are directional antennas, whose radiation pattern can be represented as [31]

$$F(\varphi, \phi) = \begin{cases} 2(\alpha + 1)\cos^\alpha \varphi, & \varphi \in [0, \frac{\pi}{2}], \\ 0, & \text{otherwise}, \end{cases} \tag{9}$$

where $2(\alpha + 1)$ is the gain of the radiation that controls the width of the beam. Here, only the main beam is considered as the direction of the antenna's radiation.

As the model considered in this paper is in the scenario of far-field, the distance between the transmitter end to the RIS and the receiver end to the RIS is much larger than the size of the surface. In order to simplify the model, let's assume that all signals are reflected by the center of the RIS. In this model, the center point of the RIS is taken as the origin, denoted as $\mathbf{q} = [0, 0]$, and the y-axis is vertical to the surface and can be regarded as the normal of the reflective surface. The coordinate of the BS and the user are denoted as $\mathbf{q}_{\text{BS}} = [X, Y]$ and $\mathbf{q}_u = [x, y]$, while φ_t and φ_r are the elevation angle of arrival (AoA) and the elevation angle of departure (AoD), respectively. The distance from the BS to the RIS is represented as D and the distance from RIS to the user is d. Based on the pathloss model given in [32], the pathloss from the BS to the RIS can be represented as

$$\varrho_t = \frac{F_t A_t}{4\pi D^2}, \tag{10}$$

where F_t is the radiation pattern from the BS antennas, and A_t is the projected aperture of the RIS toward the direction of the transmitter side. Furthermore, A_t can be expressed as $A_t = (-\mathbf{u}_y)^T (\mathbf{q}_{BS} - \mathbf{q}) s_x s_y/D$, where $\mathbf{u}_y$ is the unit vector in the y-direction, while s_x and s_y are the width and length of each element of the RIS, respectively.

The pathloss from the RIS to the user can be expressed as

$$\varrho_r = \frac{F_r A_r}{4\pi d^2}, \tag{11}$$

where F_r is the radiation pattern from the RIS antennas, and A_r denotes the projected aperture of the RIS toward the
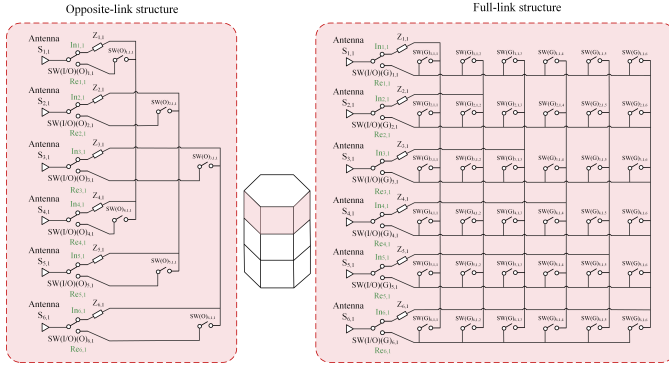
FIGURE 3. An example of the circuit design in the horizontal direction (structure 2 and 4) for the BD RIS with six sectors.

direction of the receiving end, which can be expressed as $A_r = (-\mathbf{u}_y)^T (\mathbf{q}_- \mathbf{q}_u) s_x s_y / d$.

Expanding this pathloss model into the proposed system in this paper, each user can be served by $L/2$ sectors of the RIS, as in the example of Figure 1, where the RIS has $L = 6$ sectors, and each user can be served by 3 sectors, thus having $L/2 = 3$ different pathloss values in different reflection paths. Hence, the pathloss of different sectors can be expressed by $\varrho_r = [\varrho_{r_1}, \varrho_{r_2}, \ldots, \varrho_{r_{(L/2)}}] \in \mathbb{C}^{1 \times L/2}$. Additionally, consider a sector matrix for the channel $\mathbf{H}$, denoted as $\mathbf{S}_k = [\mathbf{S}_{se_{1,k}}, \mathbf{S}_{se_{2,k}}, \ldots, \mathbf{S}_{se_{(L/2),k}}]^T \in \mathbb{C}^{L/2 \times N}$, which represents the sectors in service for the kth user, in which $\mathbf{S}_{se_{n,k}} = [s_{1,n,k}, s_{2,n,k}, \ldots, s_{L,n,k}] \in \mathbb{C}^{1 \times N}, n = 0, 1, \ldots, L/2$ and

$$s_{l,n,k} = \begin{cases} \mathbf{1}_{1 \times N_y}, & \text{the } n\text{th sector serves the } k\text{th user,} \\ \mathbf{0}_{1 \times N_y}, & \text{the } n\text{th sector does not serve the } k\text{th user.} \end{cases} \quad (12)$$

For example, in Figure 1 the n-th sector serving the user refers to one of the sector 2, 3, 4 that communicate with user k. More specifically, the channel between the RIS and the kth user can be expressed as

$$\mathbf{h}_k^H = \widetilde{\mathbf{h}}_k^H \cdot \text{Diag}\{\sqrt{\varrho_t} \mathbf{S}_k\}. \quad (13)$$

As the location of the BS is fixed, the radiation pattern gain from the BS antennas is maximized when the BS is vertical to the RIS surface. For convenience and without loss of generality, we assume that the BS always communicates with the first $L/2$ sectors, i.e. RIS sectors 1, 2, 3 in Figure 1. As the channel $\mathbf{G}$ is different in different architectures, the channel model is detailed in Section III.

In the proposed model, the signal is firstly precoded at the BS, where each user is assigned a beamforming vector, and then the multi-user precoded signal is transmitted to the RIS. Each of the RIS elements receives the multi-path signal and then combines them with the designed phase shift before reflecting them to the users.

III. RIS ARCHITECTURE

In the following, we introduce the architecture design of the different RIS structures used in this paper. We divide the

TABLE 2. RIS Structures considered in this paper.

At_H \ At_V	Independent	Non-diagonal in group with group size G_s
Independent	Structure 1 (Conv)	\
Opposite-link	Structure 2 (oppo-link)	Structure 3 (oppo-ND)
Full-link	Structure 4 (full-link)	Structure 5 (full-ND)
Structure in [29]	Structure 6 (BD-single)	\

connection methods into horizontal connections and vertical connections, which we refer to as At_H and At_V in Table 2. The horizontal connections refer to the connection between sectors, and the vertical connections refer to the connections between elements of each sector. These two connection schemes can be combined or treated independently. These different architectures can be applied to the system model of Section II, but will invoke different circuit complexity and channel gain. The RIS element connection diagram of these architectures is shown in Figure 3 and Figure 5.

A. Conventional Structure - Structure 1

Conventional (Conv) RIS structures have been proposed in [33] [34], where the elements in the RIS are not connected with each other, which means the signal is reflected from the point where it struck. In this case, when the user roams to the place that the BS can not always reach, the user cannot receive any signal. Since all elements are independent, the signal cannot be transmitted to the sector that serves the user, if the user is on the opposite side of the BS. The channel $\mathbf{G}$ for this architecture can be expressed by

$$\mathbf{G_{Conv}} = \begin{bmatrix} (\text{Diag}\{\sqrt{\varrho_t} S_G\} \cdot \widetilde{\mathbf{G}})^{1:L/2} \\ \mathbf{0}_{L/2 \times N} \end{bmatrix}. \quad (14)$$

B. Opposite-link and Full-link Structures - Structure 2 and Structure 4

In Structure 2 and 4 defined in Table 2, the elements at the corresponding positions in each sector are connected together as in Figure 3. For example, as shown in Figure 2, when $L = 2$, i.e. STAR-RIS, the user radius in $[0, 2\pi]$ can be covered by sector 1 or sector 2, but the BS is facing sector 1. So in this case, when the user is not in the same area as the BS, the channel information from the BS to the RIS can be transmitted to the sector the user is in.

Our proposed Structures 2 and 4 can ensure that users can be served no matter where they are within the service range, even when the user is in the opposite sector of the BS. The circuit design of Structure 2 (Opposite-link structure) and Structure 4 (Full-link structure) is shown in Figure 3, where in the full-link design all sectors are connected together while in the opposite-link design only sectors in opposite positions are connected together, for example sector 1 is connected to sector 4, and sector 2 is connected to sector 5 when $L = 6$.
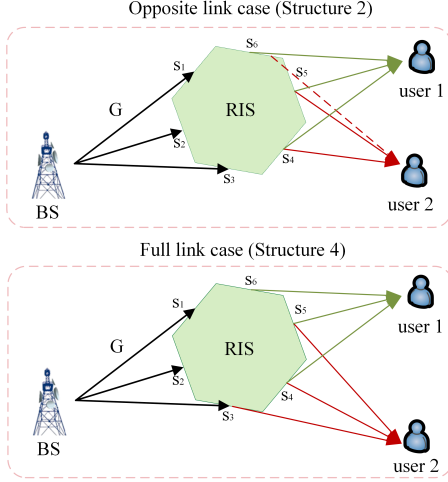
FIGURE 4. An example of serve sectors under different structures (structure 2 and 4) for the BD RIS with six sectors.

In the design of Structure 4, since the first $L/2$ sectors directly communicate with the BS, each row of the sector selection matrix corresponds to the mapping of signals from the respective incident sector to the reflected sector. In the hexagonal structure, the dimension of the sector selection matrix is $3 \times N$. For example in Figure 4, user 1 is roaming within the service area of sector 5, then the user maintains communication with sectors 4, 5, and 6, while user 2 roams within the service area of sector 4, and hence maintains communication with sectors 3, 4, and 5. The sector selection matrix under the full link case (structure 4) can be represented as

$$S^{(\text{user1})} = \begin{bmatrix} \mathbf{0}_{N_y} & \mathbf{0}_{N_y} & \mathbf{0}_{N_y} & \mathbf{1}_{N_y} & \mathbf{0}_{N_y} & \mathbf{0}_{N_y} \\ \mathbf{0}_{N_y} & \mathbf{0}_{N_y} & \mathbf{0}_{N_y} & \mathbf{0}_{N_y} & \mathbf{1}_{N_y} & \mathbf{0}_{N_y} \\ \mathbf{0}_{N_y} & \mathbf{0}_{N_y} & \mathbf{0}_{N_y} & \mathbf{0}_{N_y} & \mathbf{0}_{N_y} & \mathbf{1}_{N_y} \end{bmatrix}, \tag{15}$$

and

$$S^{(\text{user2})} = \begin{bmatrix} \mathbf{0}_{N_y} & \mathbf{0}_{N_y} & \mathbf{1}_{N_y} & \mathbf{0}_{N_y} & \mathbf{0}_{N_y} & \mathbf{0}_{N_y} \\ \mathbf{0}_{N_y} & \mathbf{0}_{N_y} & \mathbf{0}_{N_y} & \mathbf{1}_{N_y} & \mathbf{0}_{N_y} & \mathbf{0}_{N_y} \\ \mathbf{0}_{N_y} & \mathbf{0}_{N_y} & \mathbf{0}_{N_y} & \mathbf{0}_{N_y} & \mathbf{1}_{N_y} & \mathbf{0}_{N_y} \end{bmatrix}. \tag{16}$$

In each row of the sector selection matrix, the process represents the transmission of BS-RIS channel information from the first, second, and third sectors to the corresponding destination sectors, respectively.

This selection between sectors is controlled by a switch array. Let us define the switch controlling the signal on the n_yth element transmitting from the l_1th sector to the l_2th sector as $\text{SW}_{l_1, n_y, l_2}$. The sector selection matrix also describes the control problem of the switch array. The N_y elements set to 1 in the first row correspond to the connected state of the switches $\text{SW}_{1, 1 \sim N_y, 3}$, shown in Figure 3, comprising these N_y switches. Similarly, the N_y elements set to 1 in the second row correspond to the switches $\text{SW}_{2, 1 \sim N_y, 4}$, and those in the third row correspond to the switches $\text{SW}_{3, 1 \sim N_y, 5}$ being in a connected state. This configuration of the circuit
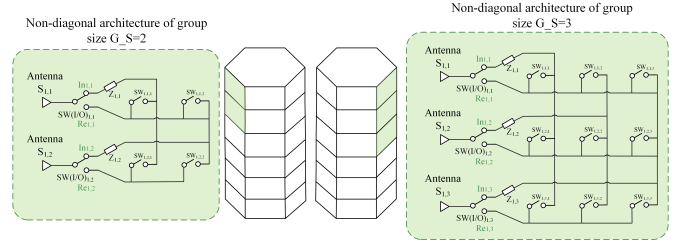

FIGURE 5. An example of the circuit design in the vertical direction (non-diagonal architecture in each group) for the BD RIS with six sectors.

connections ensures that the information transmitted from the BS to the RIS is transmitted from sectors $1 - 3$ to sectors $3 - 5$.

In Structure 2, the signal retained information on sectors $1 - 3$ will be shared with sectors $4 - 6$ correspondingly. This design enables a user to be served by either sector $1 - 3$ or sector $4 - 6$, respectively. Unlike Structure 2, the combination of sectors in Structure 2 is fixed, where the system can flexibly combine sectors according to the user's location. For example in Figure 4, when the user is within the service range of sector 4 or 5, the service sector of Structure 2 is configured as sectors $4 - 6$, which is different from the case in Structure 4. Although Structure 2 sacrifices flexibility, it achieves a simpler circuit structure than Structure 4. After information retention across the sectors, a sector selection matrix is generated based on the user's location. The switches then select and activate the reflective elements on the facet where the user is located based on this position.

Let us define S_a and S_n to describe the active status of the combined sectors for Structure 2:

$$S_{\text{a}} = \begin{bmatrix} \mathbf{1}_{N_y} & \mathbf{0}_{N_y} & \mathbf{0}_{N_y} \\ \mathbf{0}_{N_y} & \mathbf{1}_{N_y} & \mathbf{0}_{N_y} \\ \mathbf{0}_{N_y} & \mathbf{0}_{N_y} & \mathbf{1}_{N_y} \end{bmatrix}, \tag{17}$$

and

$$S_{\text{n}} = \begin{bmatrix} \mathbf{0}_{N_y} & \mathbf{0}_{N_y} & \mathbf{0}_{N_y} \\ \mathbf{0}_{N_y} & \mathbf{0}_{N_y} & \mathbf{0}_{N_y} \\ \mathbf{0}_{N_y} & \mathbf{0}_{N_y} & \mathbf{0}_{N_y} \end{bmatrix}. \tag{18}$$

Then, the sector matrix for Structure 2 case can be written as

$$S_{\text{OP}} = \begin{cases} [S_{\text{a}}, S_{\text{n}}], & \text{user served by sector } 1 - 3, \\ [S_{\text{n}}, S_{\text{a}}], & \text{user served by sector } 4 - 6, \end{cases} \tag{19}$$

where the $S_{\text{OP}} \in \mathbb{C}^{L/2 \times N}$.

In the example of Figure 4, the sector selection matrix is represented as

$$S_{\text{OP}}^{(\text{user1})} = S_{\text{OP}}^{(\text{user2})} = [S_{\text{n}}, S_{\text{a}}]. \tag{20}$$

The channel between the BS and the RIS of the Structure 2 and Structure 4 is respectively denoted as

$$\mathbf{G}_{\textbf{Stru.4}} = \left[\text{Diag}\{\sqrt{\varrho_t} S\} \cdot \widetilde{\mathbf{G}} \right], \tag{21}$$

$$\mathbf{G}_{\textbf{Stru.2}} = \left[\text{Diag}\{\sqrt{\varrho_t} S_{\text{OP}}\} \cdot \widetilde{\mathbf{G}} \right], \tag{22}$$

where $\varrho_t = [\varrho_{t1}, \varrho_{t2}, \ldots, \varrho_{L/2}] \in \mathbb{C}^{1 \times L/2}$ is the pathloss of the different transmission paths.

C. Group-connected Non-Diagonal Structure - Structure 3 and Structure 5

In Structure 2 and Structure 4, we only consider the cooperation between sectors, that is defined as horizontal structures in this work. In his section, we introduce the vertical connections as non-diagonal grouping architecture, based on [21], where we employ the non-diagonal connection scheme in each group based on the existing horizontal structure to explore further performance improvements. Structures 3 and Structure 5 defined in Table 2 are the designs that apply the vertical non-diagonal connections on the opposite-link (structure 2) and full-link (structure 4) schemes, respectively.

In the non-diagonal group-connected structure, the RIS elements in each sector are divided into different groups with group size of G_s, applying non-diagonal architecture in each group [21] [22]. In the non-diagonal structure, the phase shift matrix is not diagonal, since the signal impinging on one RIS element can be reflected from any other RIS element. A permutation matrix is needed to control the mapping sequence between the sub-channels on both ends of the RIS, corresponding to the control sequence of switches array SW, shown in Figure 3 and Figure 5.

The mapping of the element connection is based on the channels $\mathbf{H}$ and $\mathbf{G}$. For example, let us consider a MISO system, when the RIS has 6 sectors and 3 elements in each sector, and the amplitude of the channel vector $\mathbf{Gw}$ is $\{a_1, a_2, a_3\}$ with $a_1 > a_3 > a_2$, and the amplitude of the channel vector $\mathbf{h}^{\mathrm{H}}$ is $\{b_1, b_2, b_3\}$ with $b_3 > b_1 > b_2$. The mapping relationship $\mathcal{M}(i) = i'$ maps the element with the largest value in $\mathbf{g}$ to the element with largest value in $\mathbf{h}^H$, to achieve a higher channel gain [21]. Similarly, the second largest one is mapped to the second largest, and so on. Then, the mapping relationship $\mathcal{M}$ in this example becomes $\mathcal{M}(1) = 3, \mathcal{M}(2) = 2, \mathcal{M}(3) = 1$. Then, the phase shift matrix can be represented as

$$\boldsymbol{\Theta}_{(\mathrm{ND})} = \begin{bmatrix} 0 & 0 & e^{j\theta_{1,3}} \\ 0 & e^{j\theta_{2,2}} & 0 \\ e^{j\theta_{3,1}} & 0 & 0 \end{bmatrix}. \quad (23)$$

To realize the non-diagonal phase shift matrix , switches SW(I/O) are employed to switch between the receive and transmit modes for each element, enabling the mapping between elements. For example in (23), the switches $\mathrm{SW}_{1,3,1}$, $\mathrm{SW}_{1,2,2}$, and $\mathrm{SW}_{1,1,3}$ in Figure 5 are turned on and other switches are turned off. In this case, the signal received by the first element will be transmitted and reflected by the third element. The switches $\mathrm{SW(I/O)}$ are employed to switch between the receive and transmit modes for each element, where the transmit/receive mode can be configured as the channels change.

D. Beyond Diagonal Structure - Structure 6

In the works of [29] [36] [37], the authors proposed some RIS multi-section structures, where connection schemes between elements in each sector have been considered, which we refer to as vertical connection in this work. Based on their theoretical analysis, the connection schemes have similar performance upper bound as the non-diagonal scheme [21] [22], which can also reach the fully connected RIS performance upper bound [20]. In Structure 6, although the signal can be transmitted from the receiving RIS sector to the user location RIS sector, a user is only served by one sector.

In this paper, we propose Structures 2, 3, 4, 5, which are based on the cooperation between sectors, where multiple sectors refers can flexibly cooperate to serve a user.

In the example of hexagonal structure, the sector selection matrix of Structure 6 can be represented as

$$S_{\mathrm{BD}} = \begin{bmatrix} \mathbf{s}_{\mathrm{BD}_1} & \mathbf{s}_{\mathrm{BD}_2} & \mathbf{s}_{\mathrm{BD}_3} & \mathbf{s}_{\mathrm{BD}_4} & \mathbf{s}_{\mathrm{BD}_5} & \mathbf{s}_{\mathrm{BD}_6} \end{bmatrix}, \quad (24)$$

where

$$s_{\mathrm{BD}_1} = \begin{cases} \mathbf{1}_{N_y}, & \text{user served by sector } l, \\ \mathbf{0}_{N_y}, & \text{user not served by sector } l. \end{cases} \quad (25)$$

In the following section, we present the beamforming design for the above structures.

IV. BEAMFORMING DESIGN

In this section, a joint beamforming design for maximizing the achievable sum-rate is presented. This is achieved by jointly optimizing the active beamforming matrix at the BS and phase shift matrix of the RIS, where we first present the single-user case, followed by the multi-user case with users in different locations.

A. Beamforming Design for Single-user MISO system

In single-user MISO systems, the BS is equipped with M transmit antennas and the single user is equipped with a single receiver antenna, while the RIS has N elements. The system model in (1) becomes

$$y = \sqrt{P_t}\mathbf{h}^{\mathrm{H}}\boldsymbol{\Theta}\mathbf{G}\mathbf{w}x + n \quad (26)$$

and the achievable rate is given by

$$R_{\mathrm{MISO}} = \log_2\left(1 + \frac{P_t}{\sigma_n^2}\left|\mathbf{h}^{\mathrm{H}}\boldsymbol{\Theta}\mathbf{G}\mathbf{w}\right|^2\right). \quad (27)$$

The problem can be simplified to maximize the channel gain as

$$\begin{aligned} &\max_{\boldsymbol{\Theta},\mathbf{w}} \left|\mathbf{h}^{\mathrm{H}}\boldsymbol{\Theta}\mathbf{G}\mathbf{w}\right|^2, \\ \text{s.t.} \quad &\|\mathbf{w}\| = 1, \\ &0 \le \theta_i < 2\pi, \quad i = 1, 2, \ldots, N. \end{aligned} \quad (28)$$

1) Conventional and Full/Opposite-link Structure - Structure 1, Structure 2 and Structure 4

The conventional, full-link, opposite-link RIS structures, corresponding to Structure 1, Structure 2 and Structure 4 defined in Table 2, share the same beamforming scheme, as the difference between these structures has already been accounted for in the channel matrix.

Algorithm 1 AO algorithm for Structure 3 and Structure 5
_____
1: Initialize the phase shift matrix $\mathbf{\Theta}$, beamforming vector $\mathbf{w}$, and the permutation matrix $\mathbf{J}_r$ and $\mathbf{J}_t$.
for $l = 1 : L$ **do**
  2: Generate corresponding sector selection matrix $\mathbf{se}_{l,H}$ and $\mathbf{se}_{l,G}$.
  for $b = 1 : B$ **do**
    3: Generate the sub-channel $\mathbf{G}_{l,b} = \mathrm{Diag}\{\mathbf{se}_{l,G}\}\mathbf{G}_l$ and $\mathbf{H}_{l,b} = \mathrm{Diag}\{\mathbf{se}_{l,H}\}\mathbf{H}_l$
  end for
  4: Design the beamforming vector by Eq. (34).
  5: Design the elements in phase shift matrix $\mathbf{\Theta}_{l,b}$ according to the Eq. (33).
  6: Update permutation matrix $\mathbf{J}_r$ and $\mathbf{J}_t$.
  7: Continue until the maximum number of iterations is reached or the increase in the objective value is smaller than threshold ϵ.
  8: Update the optimal value of phase shift matrix $\mathbf{\Theta}_{opt,l,b}$ and $\mathbf{w}_{l,b}$.
end for
9: Update the phase shift matrix for each sector $\mathbf{\Theta}_l = \mathrm{Diag}\{\mathbf{\Theta}_{1,1}, \cdots, \mathbf{\Theta}_{l,B}\}$.
10: Output the overall phase shift matrix $\mathbf{\Theta} = \mathrm{Diag}\{\mathbf{\Theta}_1, \cdots, \mathbf{\Theta}_L\}$.
_____

The diagonal phase shift matrix $\mathbf{\Theta}$ has the ith diagonal elements given by

$$\theta_i = -\left(\angle\left[\mathbf{h}^{\mathrm{H}}\right]_i + \angle[\mathbf{Gw}]_i\right), \quad i = 1, 2, \ldots, N \quad (29)$$

and the beamforming vector $\mathbf{w}$ can be designed using Maximum Ratio Transmission (MRT) beamforming method as an example[2]:

$$\mathbf{w} = \frac{\left(\mathbf{h}^{\mathrm{H}}\mathbf{\Theta G}\right)^{\mathrm{H}}}{\|\mathbf{h}^{\mathrm{H}}\mathbf{\Theta G}\|}. \quad (30)$$

Then, we can apply alternating optimisation between $\mathbf{\Theta}$ and $\mathbf{w}$ in order to find their optimal values.

When the optimal phase shift matrix $\mathbf{\Theta}_{\mathrm{opt}}$ and beamforming vector $\mathbf{w}_{\mathrm{opt}}$ are obtained by alternating optimization (AO) method [41], the achievable rate is given by

$$R_{\mathrm{MISO}} = \log_2\left(1 + \frac{P_t}{\sigma_n^2}\left|\mathbf{h}^{\mathrm{H}}\mathbf{\Theta}_{\mathrm{opt}}\mathbf{Gw}_{\mathrm{opt}}\right|^2\right). \quad (31)$$

2) Full-link and Opposite-link Non-Diagonal Structure - Structure 3 and Structure 5

In Structure 3 and Structure 5 proposed in Section III based on [21], let us consider a RIS with L sectors and elements in each sector are divided into B groups, each with group size of G_s. The channel gain in this case can be written as

$$\left|\mathbf{h}^{\mathrm{H}}\widetilde{\mathbf{\Theta}}\mathbf{Gw}\right|^2 = \sum_{l=1}^{L}\sum_{b=1}^{B}\left|\mathbf{H}_{l,b}^{\mathrm{H}}\mathbf{J}_r\mathbf{\Theta}_{l,b}\mathbf{J}_t\mathbf{G}_{l,b}\mathbf{w}_{l,b}\right|^2, \quad (32)$$

_____
[2]Any beamforming method can be applied in practice.

where $\mathbf{J}_r \in \mathbb{C}^{N\times N}$ is a permutation matrix multiplied by the left of the column vector, which sorts the amplitude of column vector of the bth group in the lth sector $\mathbf{G}_{l,b}\mathbf{w}_{l,b}$ in ascending order. Additionally, $\mathbf{J}_t \in \mathbb{C}^{N\times N}$ is a permutation matrix multiplied by the right of the row vector, which sorts the amplitude of the row vector $\mathbf{H}_{l,b}^{\mathrm{H}}$ in ascending order. The AO algorithm is presented in Algorithm 1.

The elements in the phase shift matrix $\mathbf{\Theta}_{l,b}$ is designed as follows

$$\theta_{l,b,i} = -\left(\angle\left[\mathbf{H}_{l,b}^{\mathrm{H}}\mathbf{J}_r\right]_i + \angle[\mathbf{J}_t\mathbf{G}_{l,b}\mathbf{w}_{l,b}]_i\right), \quad i = 1, 2, \ldots, N \quad (33)$$

and the beamforming vector can be written as

$$\mathbf{w}_{l,b} = \frac{\left(\mathbf{H}_{l,b}^{\mathrm{H}}\mathbf{J}_r\mathbf{\Theta}_{l,b}\mathbf{J}_t\mathbf{G}_{l,b}\right)^{\mathrm{H}}}{\left\|\mathbf{H}_{l,b}^{\mathrm{H}}\mathbf{J}_r\mathbf{\Theta}_{l,b}\mathbf{J}_t\mathbf{G}_{l,b}\right\|}. \quad (34)$$

B. Beamforming Design for Multi-User MIMO System

In a multi-user MIMO system, the BS has M antennas communicating with K single antenna users. The system's sum rate is given by

$$\mathbf{R}_{\mathrm{MIMO}} = \sum_{k=1}^{K}\log_2\left(1 + \frac{P_t}{\sigma_n^2}\left|\mathbf{h}_k^{\mathrm{H}}\mathbf{\Theta G}\mathbf{w}_k\sqrt{\lambda_k}\right|^2\right). \quad (35)$$

Here, we aim to maximize the sum of the eigen-channel gains of all users based on the sum-path-gain maximization (SPGM) criterion [23]. The problem of maximizing the achievable rate can be written as

$$\begin{aligned}
&\max_{\mathbf{W},\mathbf{\Theta},\mathbf{\Lambda}} \sum_{k=1}^{K}\left\|\mathbf{h}_k^{\mathrm{H}}\mathbf{\Theta G}\mathbf{w}_k\sqrt{\lambda_\mathbf{k}}\right\|^2 \\
&\text{s.t.} \quad \|\mathbf{w}_k\| = 1, k = 1, 2, \ldots, K \\
&\quad\quad \lambda_1 + \ldots + \lambda_k = 1, k = 1, 2, \ldots, K \\
&\quad\quad \mathbf{\Theta} = \mathrm{Diag}\{e^{j\theta_1}, e^{j\theta_2}, \ldots, e^{j\theta_N}\} \\
&\quad\quad 0 \leq \theta_i < 2\pi, \quad i = 1, 2, \ldots, N.
\end{aligned} \quad (36)$$

There are three parameters to be optimized in (36), which is a non-convex problem and the two-stage algorithm can be used to solve it as in [21].

1) Conventional, Full-link and Opposite-link Structures - Structure 1, Structure 2 and Structure 4

In the first stage, the phase shift matrix of the RIS is optimized by maximizing the sum of the channel gain of the combined channel according to (36). This corresponds to aligning the phase between the channel from the RIS to different users and the channel from the BS to the RIS. Thus, the problem can be represented as

$$\begin{aligned}
&\max_{\mathbf{\Theta}} \sum_{k=1}^{K}\left\|\mathbf{h}_k^{\mathrm{H}}\mathbf{\Theta G}\right\|^2 \\
&\text{s.t.} \quad \mathbf{\Theta} = \mathrm{Diag}\{e^{j\theta_1}, e^{j\theta_2}, \ldots, e^{j\theta_N}\} \\
&\quad\quad 0 \leq \theta_i < 2\pi, \quad i = 1, 2, \ldots, N.
\end{aligned} \quad (37)$$

We can apply the SDR to solve this problem. By defining a column vector $\mathbf{q} = [e^{j\theta_1}, e^{j\theta_2}, \ldots, e^{j\theta_N}]^{\mathrm{T}}$, (37) can be

written as

$$
\begin{aligned}
\max_{\boldsymbol{\Theta}} \sum_{k=1}^{K} \left\| \mathbf{h}_k^{\mathrm{H}} \boldsymbol{\Theta} \mathbf{G} \right\|^2 &= \max_{\mathbf{q}} \sum_{k=1}^{K} \left\| \mathbf{q}^H \mathrm{Diag}\{\mathbf{h}_k^{\mathrm{H}}\} \mathbf{G} \right\|^2 \\
&= \max_{\mathbf{q}} \sum_{k=1}^{K} \mathbf{q}^H \boldsymbol{\Phi}_k \boldsymbol{\Phi}_k^H \mathbf{q} \\
&= \max_{\mathbf{q}} \mathbf{q}^H (\sum_{k=1}^{K} \boldsymbol{\Phi}_k \boldsymbol{\Phi}_k^H) \mathbf{q},
\end{aligned}
\tag{38}
$$

where $\boldsymbol{\Phi}_k = \mathrm{Diag}\{\mathbf{h}_k^H\} \mathbf{G}$.

Then, (38) becomes a non-convex quadratically constrained program (QCQP), which can be solved by defining $\mathbf{Q} = \mathbf{q}\mathbf{q}^H$ satisfying $\mathbf{Q} \succeq 0$ and $\mathrm{Rank}(\mathbf{Q}_{\mathrm{opt}}) = 1$. Since the rank-one constraint is non-convex, the SDR can be applied to relax the constraint, which can be written as

$$
\begin{aligned}
\max_{\mathbf{Q}} \; & \mathrm{Tr}\left(\left(\sum_{k=1}^{K} \boldsymbol{\Phi}_k \boldsymbol{\Phi}_k^{\mathrm{H}} \right) \mathbf{Q} \right) \\
\text{s.t.} \quad & \mathbf{Q} \succeq 0, \\
& |[\mathbf{Q}]_{i,i}| = 1, \quad i = 1, 2, \dots, N.
\end{aligned}
\tag{39}
$$

The optimal solution of (39) can be represented as $\mathbf{Q}_{\mathrm{opt}}$, which can be found by using some existing tools such as CVX [42]. The optimal vector can be defined from $\mathbf{Q}_{\mathrm{opt}}$ by eigenvalue decomposition as $\mathbf{q}_{\mathrm{opt}} = e^{j\angle \mathbf{P}_1}$, and $\mathbf{p}_1$ is the eigenvector corresponding to the largest eigenvalue.

2) Full-link and Opposite-link Non-Diagonal Structures - Structure 3 and Structure 5

We also apply the two-stage beamforming optimization in Structure 3 and Structure 5. However, due to users roaming randomly within the radius range, there may be cases where there are no users in service in some sectors. In the out-of-service cases, using (32) to sort the channels of users and BS may cause confusion in the multi-sector and multi-user signal transmission scenarios. As a trade-off, we can optimize the phase shift matrix of each sector, where the channel and phase shift matrix of each sector need to be evaluated separately. The phase shift matrix $\boldsymbol{\Theta}$ can be represented as

$$
\boldsymbol{\Theta} = \mathrm{Diag}\{\boldsymbol{\vartheta}_1, \boldsymbol{\vartheta}_2, \cdots, \boldsymbol{\vartheta}_L\},
\tag{40}
$$

where $\boldsymbol{\vartheta}_l \in \mathbb{C}^{N_y \times N_y}, l = 1, 2, \dots, L$ is the phase shift matrix of each sector. The channel matrix can be represented as

$$
\mathbf{h}_k^H = \begin{bmatrix}
\mathbf{h}_{1,1,1}^H & \mathbf{h}_{1,1,2}^H & \cdots & \mathbf{h}_{1,L,B}^H \\
\mathbf{h}_{2,1,1}^H & \mathbf{h}_{2,1,1}^H & & \mathbf{h}_{2,L,B}^H \\
\vdots & \vdots & \ddots & \vdots \\
\mathbf{h}_{K,1,1}^H & \mathbf{h}_{K,1,1}^H & & \mathbf{h}_{K,L,B}^H
\end{bmatrix},
\tag{41}
$$

$$
\mathbf{G} = [\mathbf{g}_{1,1}, \mathbf{g}_{1,2}, \dots, \mathbf{g}_{L,B}]^T,
\tag{42}
$$

where $\mathbf{h}_{k,l,b}^H \in \mathbb{C}^{1 \times G_s}, k = 1, 2, \dots, K, l = 1, 2, \dots, L, b = 1, 2, \dots, B$ represent the channel from the bth group in the lth sector of the RIS to the kth user, and $\mathbf{g}_{l,b} \in \mathbb{C}^{G_s \times M}$ is the channel from the BS to the bth group in the lth sector of the RIS.

In the first stage, the phase shift matrix is optimized by maximizing the sum of the channel power gain of each

sector. According to (36), the problem can be formulated as

$$
\begin{aligned}
& \sum_{l=1}^{L} \max_{\boldsymbol{\vartheta}_l} \sum_{k=1}^{K} \sum_{l=1}^{L} \sum_{b=1}^{B} \left\| \mathbf{h}_{k,l,b}^{\mathrm{H}} \boldsymbol{\vartheta}_{l,b} \mathbf{g}_{l,b} \right\|^2 \\
\text{s.t.} \quad & \boldsymbol{\vartheta}_{l,b} = \mathrm{Diag}\{e^{j\vartheta_1}, e^{j\vartheta_2}, \dots, e^{j\vartheta_{G_s}}\} \\
& 0 \le \theta_i < 2\pi, \quad i = 1, 2, \dots, N_y.
\end{aligned}
\tag{43}
$$

Then, the SDR can be applied to solve this problem. By defining a column vector $\mathbf{q}_{l,b} = [e^{j\vartheta_1}, e^{j\vartheta_2}, \dots, e^{j\vartheta_{G_s}}]^H$, (43) can be written as

$$
\begin{aligned}
& \sum_{l=1}^{L} \max_{\boldsymbol{\vartheta}_l} \sum_{k=1}^{K} \sum_{b=1}^{B} \left\| \mathbf{h}_{k,l,b}^{\mathrm{H}} \boldsymbol{\vartheta}_{l,b} \mathbf{g}_{l,b} \right\|^2 \\
&= \sum_{l=1}^{L} \sum_{k=1}^{K} \sum_{b=1}^{B} \left\| \mathbf{h}_{k,l,b}^{\mathrm{H}} \mathbf{J}_{r,l,b} \widetilde{\boldsymbol{\vartheta}}_l \mathbf{J}_{t,l,b} \mathbf{g}_{l,b} \right\|^2 \\
&= \sum_{l=1}^{L} \sum_{k=1}^{K} \sum_{b=1}^{B} \mathbf{q}_{l,b}^H \boldsymbol{\Phi}_{k,l,b} \boldsymbol{\Phi}_{k,l,b}^H \mathbf{q}_{l,b} \\
&= \sum_{l=1}^{L} \sum_{b=1}^{B} \mathbf{q}_{l,b}^H (\sum_{k=1}^{K} \boldsymbol{\Phi}_{k,l,b} \boldsymbol{\Phi}_{k,l,b}^H) \mathbf{q}_{l,b},
\end{aligned}
\tag{44}
$$

where $\boldsymbol{\Phi}_{k,l,b} = \mathrm{Diag}\{\mathbf{h}_{k,l,b}^H \mathbf{J}_{r,l,b}\} \mathbf{J}_{t,l,b} \mathbf{g}_{l,b}$, and $\boldsymbol{\Phi}_{k,l} = \mathrm{Diag}\{\boldsymbol{\Phi}_{k,l,1}, \cdots, \boldsymbol{\Phi}_{k,l,B}\}$.

The permutation matrices $\mathbf{J}_t$ and $\mathbf{J}_r$ cannot be designed as in (32), where instead of using the exhaustive search method, a sub-optimal method can be used to sort the channel amplitudes of multiple users in each sector. Explicitly, $\mathbf{J}_t$ is sorted based on the vector $\mathbf{g}_{l,b}' = \frac{1}{M} \sum_{m=1}^{M} |\mathbf{g}_{l,b,m}|$ in ascending order and $\mathbf{J}_r$ is sorted based on the vector $\mathbf{h}_l' = \frac{1}{K} \sum_{k=1}^{K} |\mathbf{h}_{k,l,b}|$ in ascending order. More specifically, the optimization problem of the phase shift matrix in each sector in (44) becomes a QCQP, which can be solved by defining $\mathbf{Q}_{l,b} = \mathbf{q}_{l,b} \mathbf{q}_{l,b}^H$ satisfying $\mathbf{Q}_{l,b} \succeq 0$ and $\mathrm{Rank}(\mathbf{Q}_{l,b,\mathrm{opt}}) = 1$. Since the rank-one constraint is non-convex, the SDR can be applied to relax the constraint, which can be written as

$$
\begin{aligned}
\max_{\mathbf{Q}_{l,b}} \; & \mathrm{Tr}\left(\left(\sum_{k=1}^{K} \boldsymbol{\Phi}_{k,l,b} \boldsymbol{\Phi}_{k,l,b}^{\mathrm{H}} \right) \mathbf{Q}_{l,b} \right) \\
\text{s.t.} \quad & \mathbf{Q}_{l,b} \succeq 0, \\
& |[\mathbf{Q}_{l,b}]_{i,i}| = 1, \quad i = 1, 2, \dots, N_y.
\end{aligned}
\tag{45}
$$

The optimal solution of $\mathbf{q}_{l,\mathrm{opt}}$ can be acquired from the optimal solution in (45), where $\mathbf{Q}_{l,b,\mathrm{opt}}$ can be eigenvalue decomposed as $\mathbf{q}_{l,b,\mathrm{opt}} = e^{j\angle \mathbf{P}_1}$, where $\mathbf{p}_1$ is the eigenvector corresponding to the largest eigenvalue. The phase shift matrix can be represented as $\boldsymbol{\vartheta}_{l,b,\mathrm{opt}} = \mathbf{J}_r \mathrm{Diag}\{\mathbf{q}_{l,b,\mathrm{opt}}\} \mathbf{J}_t$.

However, there may also be such situations that certain sectors have no users to serve. In this case, the channels in those sectors are empty. Then, we can set the phase shift matrix in these sectors as a diagonal matrix with a value of e^{j0} on the diagonal, that is $\boldsymbol{\vartheta}_{l,b} = \mathrm{Diag}\{e^{j0}, \dots, e^{j0}\} \in \mathbb{C}^{1 \times G_s}$ and $\boldsymbol{\vartheta}_l = \mathrm{Diag}\{\boldsymbol{\vartheta}_{l,1}, \dots, \boldsymbol{\vartheta}_{l,B}\} \in \mathbb{C}^{1 \times N_y}$. The phase shift matrix of the whole system $\boldsymbol{\Theta}_{\mathrm{opt}}$ is defined in (40).

In the second stage, the transmit beamforming matrix and power allocation matrix can be obtained by operating SVD method on the equivalent channel $\mathbf{H}_{\mathrm{equ}} = \mathbf{H}^{\mathrm{H}} \boldsymbol{\Theta}_{\mathrm{opt}} \mathbf{G} = \mathbf{U} \boldsymbol{\Sigma} \mathbf{V}^{\mathrm{H}}$. The transmit beamforming matrix $\mathbf{W}$ is designed based in the first K columns of $\mathbf{V}$, that is $\mathbf{W}_{\mathrm{opt}} = \mathbf{V}^{(1:K)}$. The power allocation matrix $\boldsymbol{\Lambda}$ can be calculated based on the water-filling method [35]. Finally, the achievable rate can

be represented as

$$\mathbf{R}_{\text{MIMO}} = \log_2\left(\mathbf{I} + \frac{P_t}{\sigma_n^2}\mathbf{H}_{\text{equ}}\mathbf{W}_{\text{opt}}\mathbf{\Lambda}\mathbf{W}_{\text{opt}}^H\mathbf{H}_{\text{equ}}^H\right). \quad (46)$$

V. THEORETICAL ANALYSIS FOR THE RECEIVED SIGNAL POWER

In this section, we present the theoretical analysis of our proposed RIS structure for performance analysis and hardware complexity based on SISO systems. In the following, we discuss the structure where the number of sectors in the RIS is $L \geq 2$ (even number), in which the signal is transmitted by a single-antenna transmitter, and received by a single-antenna receiver.

A. Performance analysis

In this section, we explore the enhancements offered by our newly proposed structure (Structure 5) which utilizes a group size of N_y, focusing on its performance relative to a benchmark structure (Structure 4). We examine how the unique configuration of Structure 5 amplifies the received signal power, where we derive the critical mathematical expressions to quantify this gain. The analysis reveals that Structure 5 can reduce complexity and achieves comparable or enhanced signal reception capabilities under specific conditions. These insights set the stage for a deeper dive into the mathematical underpinnings and potential applications of our findings in advanced communication systems. The received signal at the receiving side can be written as

$$\begin{aligned} y &= \sqrt{P_T}\mathbf{H}^H\mathbf{\Theta}\mathbf{G}s + n \\ &= \sqrt{P_T\varrho_t\varrho_r}\widetilde{\mathbf{H}}^H\mathbf{\Theta}\widetilde{\mathbf{G}}s + n. \end{aligned} \quad (47)$$

The corresponding received signal power can be derived as

$$\begin{aligned} P_R &= |\sqrt{P_T\varrho_t\varrho_r}\widetilde{\mathbf{H}}^H\mathbf{\Theta}\widetilde{\mathbf{G}}|^2 \\ &= P_T\varrho_t\varrho_r|\widetilde{\mathbf{H}}^H\mathbf{\Theta}\widetilde{\mathbf{G}}|^2. \end{aligned} \quad (48)$$

Since $||\mathbf{\Theta}|| = 1$, (48) can be written as

$$P_R = P_T\varrho_t\varrho_r\left(\sum_{i=1}^N[\widetilde{\mathbf{H}}^H]_i[\widetilde{\mathbf{G}}]_i\right)^2. \quad (49)$$

In Structure 4, the average value of the received power can be represented as

$$\begin{aligned} \bar{P}_R &= P_T\bar{\varrho}_t\bar{\varrho}_r\mathbb{E}\left(\left(\sum_{i=1}^N a_ib_i\right)^2\right) \\ &= P_T\bar{\varrho}_t\bar{\varrho}_r\sum_{i=1}^N\mathbb{E}(a_i^2)\mathbb{E}(b_i^2) \\ &\quad + 2\sum_{i=1}^{N-1}\sum_{j=i+1}^N\mathbb{E}(a_i)\mathbb{E}(b_i)\mathbb{E}(a_j)\mathbb{E}(b_j), \end{aligned} \quad (50)$$

where a_i and b_i represent the amplitude of the ith element in channel $\mathbf{H}$ and $\mathbf{G}$, respectively.

If we set the parameter for the Rician channel as $\kappa_{\mathbf{h}_k} = \kappa_{\mathbf{G}} = 0$, a_i and b_i follow the Rayleigh distribution and we can compute their mean values as

$$\mathbb{E}(a_i) = \mathbb{E}(b_i) = \frac{\sqrt{\pi}}{2}, \quad (51)$$

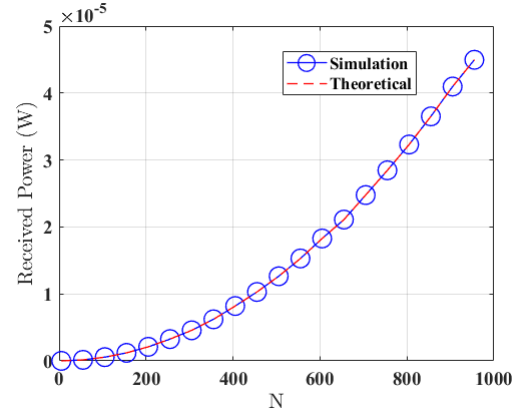$$\mathbb{E}(a_i^2) = \mathbb{E}(b_i^2) = 1. \quad (52)$$

FIGURE 6. Comparison of the achievable average power in SISO system under Rayleigh channel.

From (50), (51) and (52) we can get

$$\bar{P}_R = P_T = \bar{\varrho}_t\bar{\varrho}_r(N + N(N-1)\frac{\pi^2}{16}), \quad (53)$$

where $\bar{\varrho}_t$ and $\bar{\varrho}_r$ are the average pathloss in $\mathbf{H}$ and $\mathbf{G}$, which can be represented as

$$\bar{\varrho}_t = \frac{1}{L/2}\sum_{l=1}^{L/2}\varrho_{t_l}, \quad \bar{\varrho}_r = \frac{1}{L/2}\sum_{l=1}^{L/2}\varrho_{r_l}. \quad (54)$$

In Structure 5 with $G_s = N_y$, the average received power can be computed as

$$\begin{aligned} \bar{P}_R &= P_T\bar{\varrho}_t\bar{\varrho}_r\mathbb{E}\left(\left(\sum_{i=1}^N a_{(i)}b_{(i)}\right)^2\right) \\ &= P_T\bar{\varrho}_t\bar{\varrho}_r\sum_{i=1}^N\mathbb{E}(a_{(i)}^2)\mathbb{E}(b_{(i)}^2) \\ &\quad + 2\sum_{i=1}^{N-1}\sum_{j=i+1}^N\mathbb{E}(a_{(i)})\mathbb{E}(b_{(i)})\mathbb{E}(a_{(j)})\mathbb{E}(b_{(j)}), \end{aligned} \quad (55)$$

where $a_{(i)}$ and $b_{(i)}$ represent the sequence of the sorted value of the amplitude of channel $\mathbf{H}$ and $\mathbf{G}$ in ascending order. According to Cauchy-Schwarz inequality, (55) can be expressed as

$$\begin{aligned} \bar{P}_R &= P_T\bar{\varrho}_t\bar{\varrho}_r\mathbb{E}\left(\left(\sum_{i=1}^N a_{(i)}b_{(i)}\right)^2\right) \\ &\leq P_T\bar{\varrho}_t\bar{\varrho}_r\mathbb{E}\left(\left(\sum_{i=1}^N a_{(i)}^2\right)\left(\sum_{i=1}^N b_{(i)}^2\right)\right), \end{aligned} \quad (56)$$

where the equality sign in the above inequality is only established when $a_{(i)} = b_{(i)}$. When $N \to \infty$ we can get

$$a_{(i)} = b_{(i)} = F_{a_i}^{-1}\left(\frac{i}{N}\right) = F_{b_i}^{-1}\left(\frac{i}{N}\right), \quad (57)$$

where $F_{a_i}^{-1}(\cdot)$ and $F_{b_i}^{-1}(\cdot)$ represent the inverse CDF of $a_{(i)}$ and $b_{(i)}$. When $N \to \infty$, the average received power can be represented as

$$\begin{aligned} \bar{P}_R &= P_T\bar{\varrho}_t\bar{\varrho}_r\mathbb{E}\left(\left(\sum_{i=1}^N a_{(i)}^2\right)\left(\sum_{i=1}^N b_{(i)}^2\right)\right) \\ &= P_T\bar{\varrho}_t\bar{\varrho}_r\mathbb{E}\left(\sum_{i=1}^N a_i^2\right)\mathbb{E}\left(\sum_{i=1}^N b_i^2\right) \\ &= P_T\bar{\varrho}_t\bar{\varrho}_r N^2. \end{aligned} \quad (58)$$

Hence, when the number of RIS elements approaches infinity, Structure 5 can achieve similar rate value to the fully connected architecture. From the perspective of circuit design complexity, the proposed architecture is less intricate

TABLE 3. Number of switches used in different structures (Stru. refers to Structure defined in Table 2).

$At_H \backslash At_V$	Independent	$G_s = 2, B = N_y/2$	$G_s = 3, B = N_y/3$	$G_s = N_y, B = 1$
Opposite-link	$N_x \times N_y$ (Structure 2)	$N_x \times N_y + G_s \times N_y$ (Structure 3)	$N_x \times N_y + G_s \times N_y$ (Structure 3)	$N_x \times N_y + N_y^2$ (Structure 3)
Full-link	$N_x^2 \times N_y$ (Structure 4)	$N_x^2 \times N_y + G_s \times N_y$ (Structure 5)	$N_x^2 \times N_y + G_s \times N_y$ (Structure 5)	$N_x^2 \times N_y + N_y^2$ (Structure 5)

compared to the fully connected structure, yet it can attain a comparable performance.

In [36], the author also proposed a tree connected architecture that is also available in the BD-RIS structure for enabling similar performance as that of the fully connected architecture. The tree connected structure achieves the performance with a large number of tunable impedance components, while also requiring a lower complexity compared to the fully connected structure of [20]. On the other hand, using switches in our proposed design require a reduced energy consumption compared to the tunable impedance components [38] [39]. Relying on using RF micro-electromechanical systems (MEMS) [40], the switch array turns out to be very attractive and has been widely used in wireless communication systems because it offers near-zero power consumption, high isolation, low insertion loss, low intermodulation products and low cost solution.

In Figure 6, we plot the received power of the theoretical value derived in (58) and the simulation value under the SISO system with user roaming distance $R_D = 25$m. We can observe that the simulation average received power is the same as the upper bound for the theoretical received power value, which shows the upper bound of (58) is tight.

B. Hardware complexity

In this section, we provide a high-level comparison of hardware complexity across different RIS architectures, particularly focusing on the number of phase shifters and switches each structure requires. This analysis illustrates the significant impact of architectural choices on hardware demands, facilitating an understanding of the trade-offs involved in the practical deployment of these systems. A detailed examination of the specific hardware components used in Structures 3 and 5 highlights how varying configurations can influence the overall system efficiency and power consumption.

The number of phase shifters required by all structures proposed is $N = N_x \times N_y$. Structures 3 and 5 require different number of switches, where additional switches are required for controlling signal routing among RIS elements, which have considerable low power consumption. The hardware complexity comparison for various RIS architectures is shown in Table 3.

In the non-diagonal architecture, data experiences a sorting process based on the amplitude of the channels on both sides of the RIS. The computational complexity of sorting is determined by the number of elements in each non-diagonal group. The complexity calculation uses the general bubble sorting method, where one comparison of data is recorded as one unit of complexity. The sorting complexity in each non-diagonal group can be expressed as $G_s(G_s - 1) \times B$, where G_s represents the group size, and $B = \frac{N_y}{G_s}$ represents the number of groups divided in each sector.

Comparing the hardware complexity of Structure 3 with Structure 4, the number of switches required for these two structures are $N_x \times N_y + G_s \times N_y + G_s(G_s - 1) \times G_n$ and $N_x^2 \times N_y$, respectively. In the proposed structure, with $N_x = L = 6$, as long as the group size is $G_s \leq 15$, the hardware complexity of Structure 3 is consistently lower than that of Structure 4.

C. Directional Gains

In this section, we explore the performance benefits of our proposed multi-sector-cooperative Reconfigurable Intelligent Surface (RIS) system compared to traditional single-sector-per-user RIS configurations. By examining the influence of signal incident angles on the system pathloss and RIS radiation gain, we quantify the theoretical gains at various user angles. Our findings demonstrate the superior adaptability and efficiency of the multi-sector approach in dynamically enhancing signal quality across different user positions. This analysis lays the groundwork for understanding how multi-sector cooperation can significantly enhance system performance in realistic communication environments.

In our proposed systems, each user is jointly served by $L/2$ sectors simultaneously, whereas in [29] each user is served by only one sector. As the system pathloss and RIS radiation gain are related to the signal incident and reflection angles, we analyzed the gains brought by the multi-sector-cooperative RIS and the single-sector-per-user RIS [29], when the signal incident angle changes.

We define the x-y-z axes on the RIS structure, as shown in Figure 7. To explore the effect of changes in the angle between the user and the fixed sector's normal line, we calculate the theoretical gain difference between our proposed multi-sector-cooperative RIS and the single-sector-single-user RIS proposed in [29], at angles ϕ_1 of 0 degrees, 15 degrees, and 30 degrees. As shown in Figure 7, in the proposed multi-sector-cooperative RIS, ϕ_2 and ϕ_3 change correspondingly as the user moves. The user starts moving from the positive direction of the y-axis and rotates clockwise. A rotation matrix is used to calculate the new direction vector after rotation, which is represented as

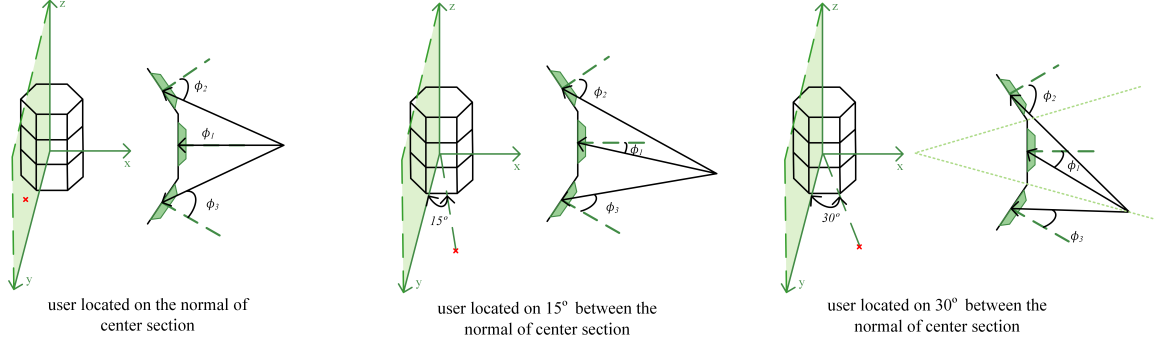$$R(t) = \begin{bmatrix} \cos(t) & \sin(t) \\ -\sin(t) & \cos(t) \end{bmatrix}. \tag{59}$$

FIGURE 7. User-RIS angular relationships.

The user's initial direction vector at $0°$ denoted as $\mathbf{v}(0°)$ on the y-axis is expressed as $[0, 1]$ here. Upon applying the rotation matrix, the user's direction vector $\mathbf{v}(t)$ at t degrees is given by

$$\mathbf{v}(t) = R(t) \cdot \begin{bmatrix} 0 \\ 1 \end{bmatrix} = \begin{bmatrix} \sin(t) \\ \cos(t) \end{bmatrix} \tag{60}$$

The normal vector of the three sectors can be represented as $\mathbf{n}_2 = [-\frac{\sqrt{3}}{2}, \frac{1}{2}]$, $\mathbf{n}_1 = [0, 1]$ and $\mathbf{n}_3 = [\frac{\sqrt{3}}{2}, \frac{1}{2}]$, respectively. As $\mathbf{v}(t)$ and $\mathbf{n}_i$ are both unit vectors, the angle between the user and each normal vector can be calculated by

$$\cos \phi_i(t) = \frac{\mathbf{v}(t) \cdot \mathbf{n}_i}{|\mathbf{v}(t)||\mathbf{n}_i|} = \mathbf{v}(t) \cdot \mathbf{n}_i. \tag{61}$$

Furthermore, the pathloss between the path from the ith sector to the user can be expressed as

$$\begin{aligned} \varrho_{\phi_i} &= \frac{F_r A_r}{4\pi d^2} = \frac{2(\alpha+1)\cos^\alpha \phi_i(-\mathbf{u}_y)^T(\mathbf{q}_-\mathbf{q}_u)s_x s_y}{4\pi d^3} \\ &= \frac{2(\alpha+1)s_x s_y}{4\pi d^3} \cos^\alpha \phi_i |\mathbf{q}_u| \cos t \\ &= f(d) \cos^\alpha \phi_i \cos t, \end{aligned} \tag{62}$$

where $f(d) = \frac{2(\alpha+1)s_x s_y}{4\pi d^3}$. Note that the pathloss gain in [29] can also be represented by ϱ_{ϕ_1} in (62).

When $t = 0°$, the user direction vector is $\mathbf{v}(0°) = [0, 1]$. The user and each sector normal angle can be represented as $\cos(\phi_2) = [0, 1] \cdot \left[-\frac{\sqrt{3}}{2}, \frac{1}{2}\right] = \frac{1}{2}$, $\cos(\phi_1) = [0, 1] \cdot [0, 1] = 1$, and $\cos(\phi_3) = [0, 1] \cdot \left[\frac{\sqrt{3}}{2}, \frac{1}{2}\right] = \frac{1}{2}$. When $\alpha = 2.5$, we have $\varrho_{\phi_2} = \varrho_{\phi_3} = 0.1768\varrho_{\phi_1} = 0.1768f(d)$.

When $t = 15°$, the user direction vector is $\mathbf{v}(15°) = [\sin(15°), \cos(15°)]$. The user and each sector normal angle can be represented as $\cos(\phi_2) = [\sin(15°), \cos(15°)] \cdot \left[-\frac{\sqrt{3}}{2}, \frac{1}{2}\right] = \sin(15°) \cdot -\frac{\sqrt{3}}{2} + \cos(15°) \cdot \frac{1}{2}$, $\cos(\phi_1) = [\sin(15°), \cos(15°)] \cdot [0, 1] = \cos(15°)$, and $\cos(\phi_3) = [\sin(15°), \cos(15°)] \cdot \left[\frac{\sqrt{3}}{2}, \frac{1}{2}\right] = \sin(15°) \cdot \frac{\sqrt{3}}{2} + \cos(15°) \cdot \frac{1}{2}$. When $\alpha = 2.5$, $\varrho_{\phi_1} \approx 0.886f(d)$, $\varrho_{\phi_3} \approx 0.389f(d)$ and $\varrho_{\phi_2} \approx 0.032f(d)$.

When $t = 30°$, the user direction vector is $\mathbf{v}(30°) = [\sin(30°), \cos(30°)]$. The user and each sector normal angle can be represented as $\cos(\phi_2) = [\sin(30°), \cos(30°)] \cdot \left[-\frac{\sqrt{3}}{2}, \frac{1}{2}\right] = \frac{1}{2} \cdot -\frac{\sqrt{3}}{2} + \frac{\sqrt{3}}{2} \cdot \frac{1}{2} = 0$, $\cos(\phi_1) = [\sin(30°), \cos(30°)] \cdot [0, 1] = \frac{\sqrt{3}}{2}$, and $\cos(\phi_3) =$
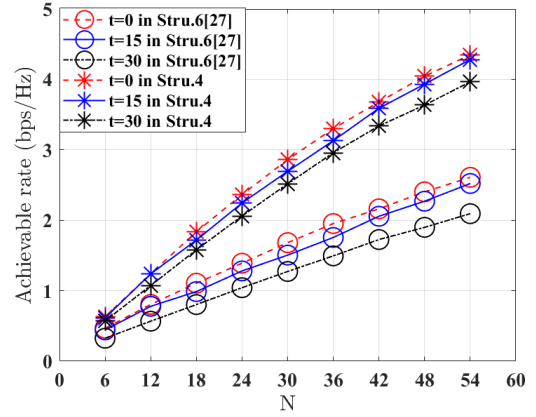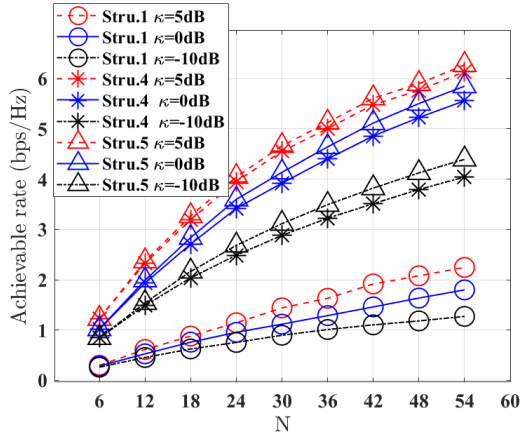

FIGURE 8. Comparison of the achievable rate in SISO system, when varying the user angle and in different RIS structures (Stru. refers to Structure defined in Table 2).

$[\sin(30°), \cos(30°)] \cdot \left[\frac{\sqrt{3}}{2}, \frac{1}{2}\right] = \frac{1}{2} \cdot \frac{\sqrt{3}}{2} + \frac{\sqrt{3}}{2} \cdot \frac{1}{2} = \frac{\sqrt{3}}{2}$. When $\alpha = 2.5$, we have $\varrho_{\phi_2} = \varrho_{\phi_3} \approx 0.604f(d)$, and $\varrho_{\phi_1} = 0$.

Based on the analysis above, it is evident that when the user's position projection aligns precisely with the central sector's normal, the bilateral side sectors can provide less than one-fifth of the performance enhancement relative to the central sector. However, when the angle between the user's position projection and the central sector's normal is $15°$, the nearer side sector can contribute up to two-thirds of the performance support of the central sector. When the user's projection position is at the edge of the central sector's service range, i.e., the angle with the central sector's normal is 30 degrees, the nearer side sector can provide performance support equivalent to that of the central sector. Therefore, when users roam randomly in various directions, the multi-sector-cooperative RIS system can offer a better overall rate than a RIS system where each user is served by only a single sector. Figure 8 presents the simulation results showing how the number of RIS elements varies as users roam at different angles and distances, with $d = 30$m, when the BS antenna $M = 1$ and $\alpha = 2.5$. Figure 8 compares the multi-sector cooperative RIS system with a single-sector-single-user RIS scheme, which further supports our performance analysis above.
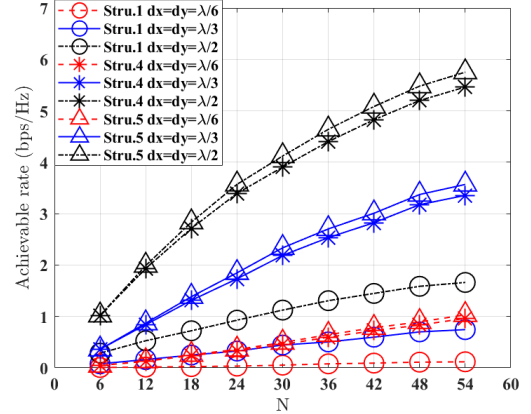
TABLE 4. Parameters Used in Simulation

Parameters	Function
L	Number of sectors in RIS
M	Number of antennas at BS
N	Number of elements in RIS
P_t	Total transmit power (mW)
σ_n^2	Noise power (dBm)
α	Beam factor in radiation pattern function
D	The largest dimension of the radiator (m^2)
d_x, d_y	Size of each element along the x-axis and y-axis (m)
d_1	Distance from BS to the center of RIS structure (m)
R_D	Roaming distance of users (m)
λ	Wave length (m)
κ	Racian factor of the fading channel (dB)

FIGURE 10. Comparison of the achievable rate in MISO system, when varying the size of RIS elements and the RIS architecture.

FIGURE 9. Comparison of the achievable rate in MISO system, when varying the Rician factor and the RIS architecture.
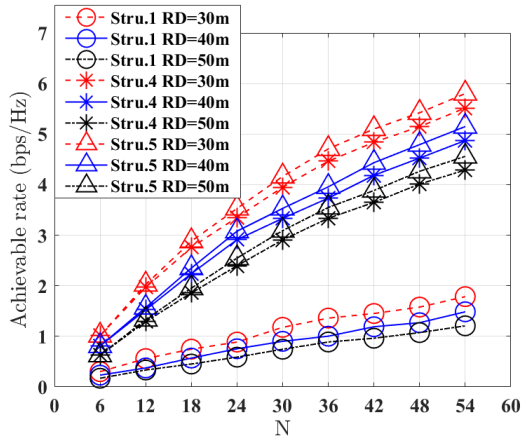
FIGURE 11. Comparison of the achievable rate in MISO system, when varying the user radius distance and the RIS architecture.

VI. SIMULATION RESULT

In this section, we present the simulation results of the achievable rate of our proposed RIS architecture ($L = 6$), compared with the STAR RIS architecture ($L = 2$) and conventional RIS architecture for different connection structures. The Monte-Carlo method is used with 10^5 iterations. The parameters used in the simulation are listed in Table 4.

The simulation results in Figure 9 to Figure 15 show the performance for the single-user MISO system, while in Figure 17 we compare the average achievable rate of each user versus the number of total RIS elements with different connection schemes in the multi-user MIMO case. The result in Figure 16 compares the hardware complexity of the different proposed structures. The abbreviation 'Stru.' in the simulations results figures refers to the structures defined in Table 2. In our simulations, the number of antennas at the BS is $M = 4$, the distance from the BS to the center of the RIS structure is $d_1 = 51$m, the total transmit power is $P_t = 50$mW, the noise power is $\sigma_n^2 = -90$dBm, and the beam factor in the radiation pattern function is $\alpha = 2.5$ [32]. We denote the total number of elements in the RIS as N, and the size of each element along the x-axis and y-axis is d_x and d_y, respectively.

In Figure 9, we compare the achievable rate versus the number of RIS elements with different Rician factor κ and different connection schemes, where the size of the RIS elements is $d_x = d_y = \lambda/2$ and the user radius distance is $R_D = 30$m. We can observe that the proposed Structure 5 with $G_s = N_y$ can perform better than the Structure 4 and Structure 1. When the Rician factor increases from -10dB to 5dB, the power of the LoS component increases, and the performance gain of the GC-ND architecture decreases, albeit still better than the other two structures.

In Figure 10, we compare the achievable rate versus the number of RIS elements with different element sizes under different connection schemes, where the user radius distance is $R_D = 30$m and the Rician factor is $\kappa_{\mathbf{G}} = \kappa_{\mathbf{h}_k} = 0$dB. Observe that structure 5 with $G_s = N_y$ performs better than Structure 4 and Structure 1. Furthermore, as the size of the RIS element increases, the channel has a lower pathloss under the same elevation angle, thus providing a higher achievable rate.

In Figure 11, we set the Rician factor of the fading channel as $\kappa_{\mathbf{G}} = \kappa_{\mathbf{h}_k} = 0$dB and the size of the RIS elements as $d_x = d_y = \lambda/2$, where we can observe that all schemes have a better performance when the user is closer to the RIS due
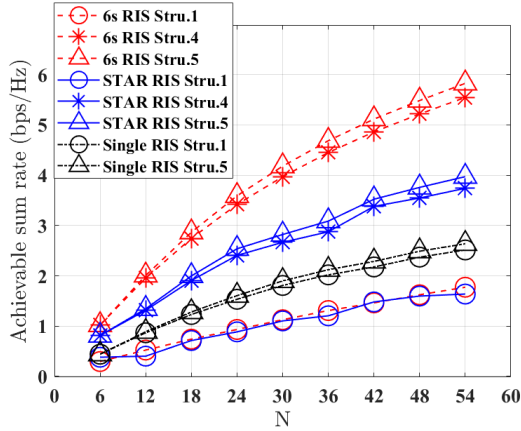
FIGURE 12. Comparison of the achievable rate in MISO system, when varying the RIS structures.
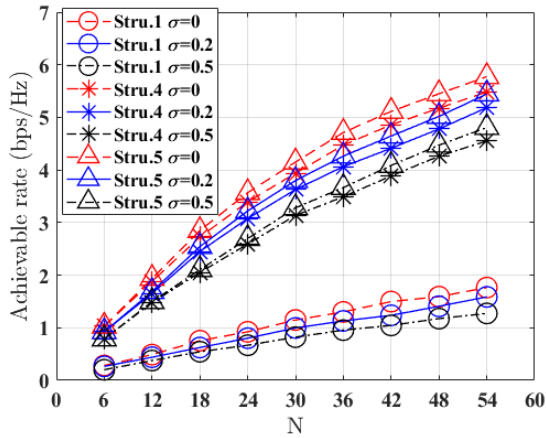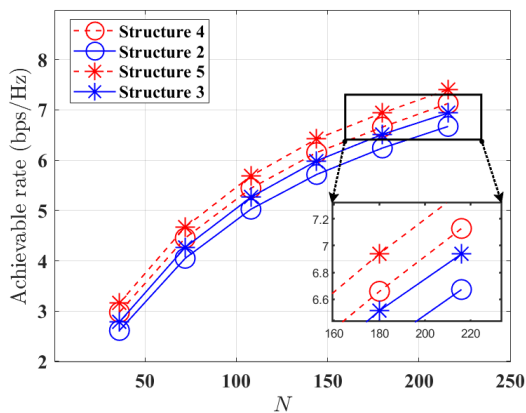

FIGURE 13. Comparison of the achievable rate in MISO system, when varying the channel estimation error and the RIS architecture.

to a lower pathloss. Furthermore, user radius distance has almost no effect on the gain of Structure 5 over the other two structures.

In Figure 12 we compare the achievable rate versus the number of RIS elements with different connection schemes under different RIS structures. In this simulation, the user ra-

FIGURE 14. Comparison of the achievable rate in MISO system, varying the RIS structures when $G_s = 3$.
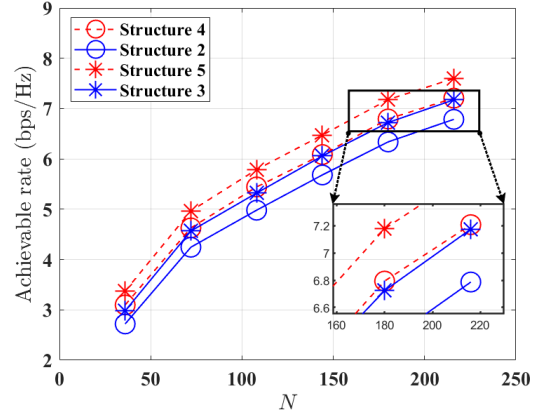

FIGURE 15. Comparison of the achievable rate in MISO system, varying the RIS structures when $G_s = 6$.

dius distance is $R_D = 30m$, the Rician factor is $\kappa_{\mathbf{G}} = \kappa_{\mathbf{h}_k} = 0$dB, and the size of the RIS elements is $d_x = d_y = \lambda/2$. We can observe that our proposed RIS structure outperforms the STAR RIS and the conventional RIS with $L = 1$, which has label 'Single RIS' in the figure. In our proposed RIS scheme, the user roams in all directions, while the user in the conventional flat RIS structure can only roam within the semicircle range facing the RIS. This means that the proposed RIS can provide higher channel capacity, while supporting users roaming in all directions.

In Figure 13, when considering imperfect Channel State Information (CSI), the channel estimates from the BS to RIS and RIS to user are represented by $\hat{g}_m = g_m + g_{m,e}$ and $\hat{h}_k^H = h_k^H + h_{k,e}^H$, respectively, for $m = 1, 2, \ldots, M$ and $k = 1, 2, \ldots, K$. The channel estimation error components $g_{m,e}$ and $h_{k,e}^H$ both follow a complex normal distribution $\mathcal{CN}(0, \sigma I)$, where σ denotes the variance of the estimation error [43] [44]. As demonstrated in Figure 13, the performance of our proposed RIS architecture surpasses that of the conventional RIS design across all considered values of the channel estimation error variance σ. This highlights the superior robustness and effectiveness of our proposed structures.

The simulation results shown in Figure 14 and Figure 15 are related to the single-user MISO system. In Figure 14 and Figure 15 we compare the average achievable rate of each user versus the number of total RIS elements under different connection schemes in the single-user MISO case with group size in each sector given by $G_s = 3$ and $G_s = 6$, respectively. In this simulation, the user radius distance is $R_D = 15m$, the Rician factor is $\kappa_{\mathbf{G}} = \kappa_{\mathbf{h}_k} = 0$dB, and the size of the RIS elements is $d_x = d_y = \lambda/2$. We can observe that Structure 5 achieves the best performance, while Structures 3 and 4 perform similar in both $G_s = 3$ and $G_s = 6$ cases. From Figure 14 and Figure 15 we can see that as the group size G_s increases, the number of elements in each vertical group also increases. In (58), we established the relationship between the number of elements and the average receive power within a non-diagonal
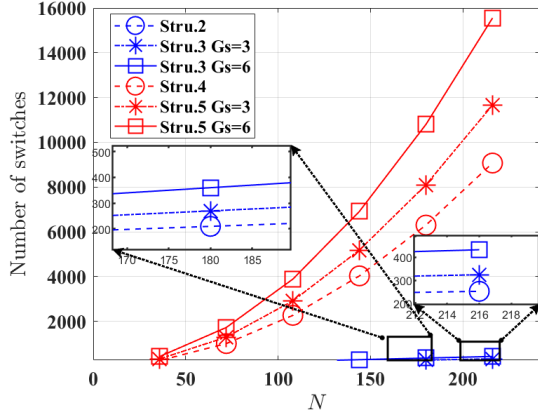
FIGURE 16. Comparison of number of switching elements integrated in the system, when varying the RIS architecture (Stru. refers to Structure defined in Table 2).
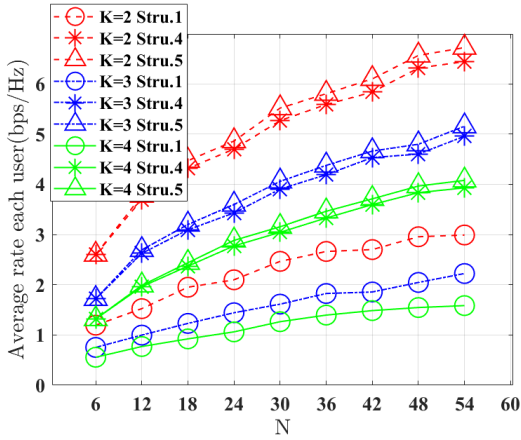

FIGURE 17. Comparison of the average rate in multi-user MIMO system, when varying the number of users and the RIS architecture (Stru. refers to Structure defined in Table 2).

group-connected architecture. It can be concluded that the performance enhances with the addition of more elements in the group, as this provides greater flexibility in the mapping. However, this also leads to a more complex circuit design due to the increased group size. The hardware complexity of these proposed structures are compared in Figure 16.

In Figure 16, we compare the number of switches integrated in each structure. As seen from Figure 14 and Figure 15 we can find that the Structure 3 can achieve a similar performance to that of Structure 4, while the hardware complexity of both structures can differ by over twenty times as shown in Figure 16. This illustrates that our proposed structure can achieve a similar average rate performance as the benchmark schemes, while greatly reducing system hardware complexity.

In Figure 17, we compare the average rate versus the number of RIS elements with different numbers of users in MIMO system. Here, the number of antennas at the BS is $M = 6$, the user radius distance is $R_D = 30$m, the Rician

factor is $\kappa_{\mathbf{G}} = \kappa_{\mathbf{h}_k} = 0$dB, and the size of each RIS element is $d_x = d_y = \lambda/2$. We can observe that the average rate of all systems increases with the number of users. Our proposed scheme has a higher average rate per user compared to the other schemes across the board.

VII. CONCLUSION

In this paper, we proposed novel RIS architectures based on the beyond diagonal RIS structure, with their corresponding circuit designs, switch array control matrices, and beamforming designs. Based on these models, we compared the system rates, circuit complexity, and gains provided by different architectures, when the users and the RIS are in various positions. We also jointly optimized the transmit beamforming and phase shift matrix for single-user MISO systems and multi-user MIMO systems using AO and SDR methods. Additionally, through theoretical analysis, we proved that the performance of the proposed Structure 5 closely approximates that of the fully connected RIS architecture. Moreover, the simulation results verified that the performance of the proposed Structure 3 can achieve similar system rate performance while significantly reducing the system hardware complexity compared to that of Structure 4.

REFERENCES

[1] Q. Wu, S. Zhang, B. Zheng, C. You and R. Zhang, "Intelligent Reflecting Surface-Aided Wireless Communications: A Tutorial," *IEEE Trans. Commun.*, vol. 69, no. 5, pp. 3313-3351, May 2021.

[2] Y. Liu et al., "Reconfigurable Intelligent Surfaces: Principles and Opportunities," *IEEE Commun. Surv. Tutor*, vol. 23, no. 3, pp. 1546-1577, May 2021.

[3] M. Di Renzo et al., "Smart Radio Environments Empowered by Reconfigurable Intelligent Surfaces: How It Works, State of Research, and The Road Ahead," *IEEE J. Sel. Areas Commun.*, vol. 38, no. 11, pp. 2450-2525, Nov. 2020.

[4] S. Kisseleff, W. A. Martins, H. Al-Hraishawi, S. Chatzinotas and B. Ottersten, "Reconfigurable Intelligent Surfaces for Smart Cities: Research Challenges and Opportunities," *IEEE Open J.*, vol. 1, pp. 1781-1797, Nov. 2020.

[5] T. Ji, M. Hua, C. Li, Y. Huang and L. Yang, "Intelligent Reflecting Surface Enhanced Full-Duplex Wireless-Powered Communication Network," presented at *ICC 2023 - IEEE International Conference on Communications*, Rome, Italy, 2023.

[6] H. Guo, Y. -C. Liang, J. Chen and E. G. Larsson, "Weighted Sum-Rate Maximization for Intelligent Reflecting Surface Enhanced Wireless Networks," presented at *2019 IEEE Global Communications Conference (GLOBECOM)*, Waikoloa, HI, USA, 2019.

[7] B. Ning, Z. Chen, W. Chen and J. Fang, "Beamforming Optimization for Intelligent Reflecting Surface Assisted MIMO: A Sum-Path-Gain Maximization Approach," *IEEE Wirel. Commun. Le.*, vol. 9, no. 7, pp. 1105-1109, July 2020.

[8] Q. Wu and R. Zhang, "Intelligent Reflecting Surface Enhanced Wireless Network via Joint Active and Passive Beamforming," *IEEE Trans. Commun.*, vol. 18, no. 11, pp. 5394-5409, Nov. 2019.

[9] Y. Yang, S. Zhang and R. Zhang, "IRS-Enhanced OFDM: Power Allocation and Passive Array Optimization," presented at *2019 IEEE Global Communications Conference (GLOBECOM)*, Waikoloa, HI, USA, 2019, pp. 1-6.

[10] K. Feng, Q. Wang, X. Li and C. -K. Wen, "Deep Reinforcement Learning Based Intelligent Reflecting Surface Optimization for MISO Communication Systems," *IEEE Wirel. Commun. Le.*, vol. 9, no. 5, pp. 745-749, May 2020.

[11] C. Huang, G. C. Alexandropoulos, C. Yuen and M. Debbah, "Indoor Signal Focusing with Deep Learning Designed Reconfigurable Intelli-

gent Surfaces," presented at *2019 IEEE 20th International Workshop on Signal Processing Advances in Wireless Communications (SPAWC)*, Cannes, France, 2019, pp. 1-5.

[12] J. Xu, Y. Liu, X. Mu and O. A. Dobre, "STAR-RISs: Simultaneous Transmitting and Reflecting Reconfigurable Intelligent Surfaces," *IEEE Commun. Lett.*, vol. 25, no. 9, pp. 3134-3138, Sept. 2021.

[13] Y. Liu, X. Mu, J. Xu, R. Schober, Y. Hao, H. Vincent Poor, L. Hanzo, "STAR: Simultaneous transmission and reflection for 360∘ coverage by intelligent surfaces," *IEEE Wireless Commun.*, 2021. [Online]. Available: http://arxiv.org/abs/2103.09104.

[14] M. Ahmed Abdul Wahid, S. Shariq Laique, W. Ullah Khan, A. Ihsan, F. Xu, S. Chatzinotas, Z. Han, "A Survey on STAR-RIS: Use Cases, Recent Advances, and Future Research Challenges," *IEEE Internet Things J.*, vol. 10, no. 16, pp. 14689-14711, 15 Aug. 2023.

[15] X. Guo, Y. Chen and Y. Wang, "Wireless Beacon Enabled Hybrid Sparse Channel Estimation for RIS-Aided mmWave Communications," *IEEE Trans. Commun.*, vol. 71, no. 5, pp. 3144-3160, May 2023.

[16] Y. Chen, Y. Wang, Z. Wang and P. Zhang, "Robust Beamforming for Active Reconfigurable Intelligent Omni-Surface in Vehicular Communications," *IEEE J. Sel. Areas Commun.*, vol. 40, no. 10, pp. 3086-3103, Oct. 2022

[17] M. Di Renzo, A. Zappone, M. Debbah, M. Alouini, C. Yuen, J. de Rosny, S. Tretyakov, "Smart Radio Environments Empowered by Reconfigurable Intelligent Surfaces: How It Works, State of Research, and The Road Ahead," *IEEE J. Sel. Areas Commun*, vol. 38, no. 11, pp. 2450-2525, Nov. 2020.

[18] W. Tang, X. Chen, M. Chen, J. Dai, Y. Han, M. Di Renzo, S. Jin, Q. Cheng, T. Cui, "Path Loss Modeling and Measurements for Reconfigurable Intelligent Surfaces in the Millimeter-Wave Frequency Band," *IEEE Trans. Commun.*, vol. 70, no. 9, pp. 6259-6276, Sept. 2022.

[19] J. Jeong, J. H. Oh, S. Y. Lee, Y. Park and S. -H. Wi, "An Improved Path-Loss Model for Reconfigurable-Intelligent-Surface-Aided Wireless Communications and Experimental Validation," *IEEE Access*, vol. 10, pp. 98065-98078, Sept. 2022.

[20] S. Shen, B. Clerckx and R. Murch, "Modeling and Architecture Design of Reconfigurable Intelligent Surfaces Using Scattering Parameter Network Analysis," *IEEE Trans. Commun.*, vol. 21, no. 2, pp. 1229-1243, Feb. 2022.

[21] Q. Li, M. El-Hajjar, I. Hemadeh, A. Shojaeifard, A. A. M. Mourad, B. Clerckx, L. Hanzo, "Reconfigurable Intelligent Surfaces Relying on Non-Diagonal Phase Shift Matrices," *IEEE Trans. Veh. Technol.*, vol. 71, no. 6, pp. 6367-6383, June 2022.

[22] Q. Li, M. El-Hajjar, I. Hemadeh, A. Shojaeifard and L. Hanzo, "Coordinated Reconfigurable Intelligent Surfaces: Non-Diagonal Group-Connected Design," *IEEE Trans. Veh. Technol.*, Mar. 2024.

[23] B. Ning, Z. Chen, W. Chen and J. Fang, "Beamforming Optimization for Intelligent Reflecting Surface Assisted MIMO: A Sum-Path-Gain Maximization Approach," *IEEE Wirel. Commun. Le.*, vol. 9, no. 7, pp. 1105-1109, July 2020.

[24] Q. Li, M. El-Hajjar, I. Hemadeh, D. Jagyasi, A. Shojaeifard and L. Hanzo, "Performance Analysis of Active RIS-Aided Systems in the Face of Imperfect CSI and Phase Shift Noise," *IEEE Trans. Veh. Technol.*, vol. 72, no. 6, pp. 8140-8145, June 2023.

[25] Q. Li, M. El-Hajjar, I. Hemadeh, A. Shojaeifard and L. Hanzo, "Low-Overhead Channel Estimation for RIS-Aided Multi-Cell Networks in the Presence of Phase Quantization Errors," *IEEE Trans. Veh. Technol.*, vol. 73, no. 5, pp. 6626-6641, May 2024.

[26] L. Wei, C. Huang, G. C. Alexandropoulos and C. Yuen, "Parallel Factor Decomposition Channel Estimation in RIS-Assisted Multi-User MISO Communication," present at *IEEE 11th Sensor Array and Multichannel Signal Processing Workshop (SAM)*, pp. 1-5, Hangzhou, China, 2020.

[27] J. Singh, S. Srivastava, A. K. Jagannatham and L. Hanzo, "Joint Transceiver and Reconfigurable Intelligent Surface Design for Multiuser mmWave MIMO Systems Relying on Non-Diagonal Phase Shift Matrices," *IEEE Open J. Commun. Soc.*, vol. 4, pp. 2897-2912, Oct. 2023.

[28] E. Björnson and L. Sanguinetti, "Rayleigh Fading Modeling and Channel Hardening for Reconfigurable Intelligent Surfaces," *IEEE Wirel. Commun. Le.*, vol. 10, no. 4, pp. 830-834, April 2021.

[29] H. Li, S. Shen and B. Clerckx, "Beyond Diagonal Reconfigurable Intelligent Surfaces: A Multi-Sector Mode Enabling Highly Directional Full-Space Wireless Coverage," *IEEE J. Sel. Areas Commun*, vol. 41, no. 8, pp. 2446-2460, Aug. 2023.

[30] Q. Li, M. El-Hajjar, I. Hemadeh, D. Jagyasi, A. Shojaeifard, E. Basar, L. Hanzo, "The Reconfigurable Intelligent Surface-Aided Multi-Node IoT Downlink: Beamforming Design and Performance Analysis," *IEEE Internet Things J.*, vol. 10, no. 7, pp. 6400-6414, April, 2023.

[31] W. L. Stutzman and G. A. Thiele, *Antenna Theory Design, 3*rd ed. New York, NY, USA: Wiley, 2012.

[32] S. Zeng, H. Zhang, B. Di, H. Qin, X. Su and L. Song, "Reconfigurable Refractive Surfaces: An Energy-Efficient Way to Holographic MIMO," *IEEE Commun. Lett.*, vol. 26, no. 10, pp. 2490-2494, Oct. 2022.

[33] N. Souto and J. C. Silva, "Joint Beamforming Algorithm for Multi-Stream MIMO Systems Assisted by Multiple Reconfigurable Intelligent Surfaces,"*IEEE Open J. Commun. Soc.*, vol. 4, pp. 1317-1333, June 2023.

[34] S. Abeywickrama, R. Zhang, Q. Wu and C. Yuen, "Intelligent Reflecting Surface: Practical Phase Shift Model and Beamforming Optimization," *IEEE Trans. Commun.*, vol. 68, no. 9, pp. 5849-5863, Sept. 2020.

[35] Goldsmith A., *Wireless Communications*, Cambridge University Press, 2005.

[36] M. Nerini, S. Shen, H. Li and B. Clerckx, "Beyond Diagonal Reconfigurable Intelligent Surfaces Utilizing Graph Theory: Modeling, Architecture Design, and Optimization," *IEEE Trans. Commun.*, Feb. 2024.

[37] H. Li, S. Shen and B. Clerckx, "Beyond Diagonal Reconfigurable Intelligent Surfaces: From Transmitting and Reflecting Modes to Single-, Group-, and Fully-Connected Architectures," *IEEE Trans. Commun.*, vol. 22, no. 4, pp. 2311-2324, April 2023.

[38] S. Payami, N. M. Balasubramanya, C. Masouros, and M. Sellathurai, "Phase shifters versus switches: An energy efficiency perspective on hybrid beamforming," *IEEE Wireless Commun. Lett.*, vol. 8, no. 1, pp. 13-16, Feb. 2019.

[39] A. Garcia-Rodriguez, V. Venkateswaran, P. Rulikowski, and C. Masouros, "Hybrid analog-digital precoding revisited under realistic RF modeling," *IEEE Wireless Commun. Lett.*, vol. 5, no. 5, pp. 528-531, Oct. 2016.

[40] G. M. Rebeiz and J. B. Muldavin, "RF MEMS switches and switch circuits," *IEEE Microw. Mag.*,vol. 2, no. 4, pp. 59-71, Dec. 2001.

[41] Q. Wu and R. Zhang, "Intelligent Reflecting Surface Enhanced Wireless Network via Joint Active and Passive Beamforming," *IEEE Trans. Commun.*, vol. 18, no. 11, pp. 5394-5409, Nov. 2019.

[42] M. Grant, S. Boyd, and Y. Ye, "CVX: MATLAB software for disciplined convex programming," 2008, [Online]. Available: http://www.stanford. edu/boyd/cvx/.

[43] S. Katla, L. Xiang, Y. Zhang, M. El-Hajjar, A. A. M. Mourad and L. Hanzo, "Deep Learning Assisted Detection for Index Modulation Aided mmWave Systems," in IEEE Access, vol. 8, pp. 202738-202754, Nov. 2020.

[44] Z. Linfu, P. Zhiwen, A. A. Ahmad, H. Dahrouj and M. El-Hajjar, "Joint Beamforming and Combining Design for mmWave Integrated Access and Backhaul Networks," in IEEE Open Journal of the Communications Society, vol. 5, pp. 503-513, Jan. 2024.